Phase structure of two-color QCD at real and imaginary chemical potentials: Lattice simulations and model analyses

Takahiro Makiyama,[1,*] Yuji Sakai,[2,†] Takuya Saito,[3,‡] Masahiro Ishii,[4,§] Junichi Takahashi,[4,‖] Kouji Kashiwa,[5,¶] Hiroaki Kouno,[1,**] Atsushi Nakamura,[6,††] and Masanobu Yahiro[4,‡‡]

[1]*Department of Physics, Saga University, Saga 840-8502, Japan*
[2]*Riken, Saitama 351-0198, Japan*
[3]*Integrated Information Center, Kochi University, Kochi 780-8520, Japan*
[4]*Department of Physics, Graduate School of Sciences, Kyushu University, Fukuoka 812-8581, Japan*
[5]*Yukawa Institute for Theoretical Physics, Kyoto University, Kyoto 606-8502, Japan*
[6]*School of Biomedicine, Far Eastern Federal University, Sukhanova 8, Vladivostok 690950, Russia; Research Center for Nuclear Physics, Osaka University, Ibaraki, Osaka 567-0047, Japan; Theoretical Research Division, Nishina Center, RIKEN, Wako 351-0198, Japan and RIISE, Hiroshima University, Higashi-Hiroshima, Hiroshima 739-8521, Japan*

(Received 16 February 2015; revised manuscript received 23 October 2015; published 14 January 2016)

We investigate the phase structure of two-color QCD at both real and imaginary chemical potentials (μ), performing lattice simulations and analyzing the data with the Polyakov-loop extended Nambu–Jona-Lasinio (PNJL) model. Lattice QCD simulations are done on an $8^3 \times 4$ lattice with the clover-improved two-flavor Wilson fermion action and the renormalization-group-improved Iwasaki gauge action. We test the analytic continuation of physical quantities from imaginary μ to real μ by comparing lattice QCD results calculated at real μ with the results of an analytic function, the coefficients of which are determined from lattice QCD results at imaginary μ. We also test the validity of the PNJL model by comparing model results with lattice QCD ones. The PNJL model is good in the deconfinement region, but less accurate in the transition and confinement regions. This problem is cured by introducing the baryon degree of freedom to the model. It is also found that the vector-type four-quark interaction is necessary to explain lattice data on the quark number density.

DOI: 10.1103/PhysRevD.93.014505

I. INTRODUCTION

Exploration of QCD phase diagrams is one of the most important subjects in not only nuclear and particle physics but also cosmology and astrophysics. However, due to the complexity of fermion determinants, the first-principles calculation, i.e., lattice QCD (LQCD) simulations, are quite difficult at high-quark-number chemical potential μ. The QCD partition function Z at finite temperature T and finite μ is expressed by

$$Z = \int DU \det[M(\mu)] e^{-S_{\rm G}}, \tag{1}$$

where U_μ ($\mu = 1, 2, 3, 4$) and $S_{\rm G}$ are the link variables and the pure gauge action, respectively, and $M(\mu)$ is written as

$$M(\mu) = \gamma_\mu D_\mu + m - \mu\gamma_4, \tag{2}$$

with the covariant derivative D_μ and the quark mass m in the continuum limit. For later convenience, we regard μ as a complex variable. It is easy to verify that

$$\{\det[M(\mu)]\}^* = \det[M(-\mu^*)]. \tag{3}$$

Hence, the fermion determinant $\det[M(\mu)]$ is not real when μ is real, and the importance sampling technique does not work in the Monte Carlo simulations there. This is the well-known sign problem. Several methods were proposed so far to resolve this problem; these are the reweighting method [1], the Taylor expansion method [2,3], the analytic continuation from imaginary μ to real μ [4–11], the complex Langevin method [12–14], and the Lefschetz thimble theory [15,16]. However, at present, these are still far from perfection.

On the contrary, in two-color QCD ($\mathrm{QC_2D}$), the lattice simulations can be made at real and finite μ, since the theory has no sign problem [17–23]. In fact, the following relation is obtained:

$$\det[M(\mu)] = \det[(t_2 C\gamma_5)^{-1} M(\mu)(t_2 C\gamma_5)] = (\det[M(\mu^*)])^*, \tag{4}$$

where t_2 and $C = \gamma_2\gamma_4$ are the second Pauli matrix in color space and the charge conjugation matrix, respectively.

*12634019@edu.cc.saga-u.ac.jp
†ysakai@riken.jp
‡tsaitou@kochi-u.ac.jp
§ishii@email.phys.kyushu-u.ac.jp
‖takahashi@phys.kyushu-u.ac.jp
¶kouji.kashiwa@yukawa.kyoto-u.ac.jp
**kounoh@cc.saga-u.ac.jp
††nakamura@riise.hiroshima-u.ac.jp
‡‡yahiro@phys.kyushu-u.ac.jp

Obviously, $\det[M(\mu)]$ is real when μ is real. Recently, Hands *et al.* analyzed the phase structure of QC_2D in a wide range of real μ by using two-flavor Wilson fermions [21,22]. QC_2D can also be used to check the validity of methods proposed to resolve the sign problem. In fact, Giudice and Papa and Cea *et al.* [24–26] tested the validity of analytic continuation from imaginary μ to real μ with staggered fermions.

Equation (3) shows that $\det[M(\mu)]$ is real when μ is pure imaginary, i.e., $\mu = i\mu_I = i\theta T$ for real variables μ_I and θ, so that LQCD simulations are feasible there. Observables at real μ are extracted from those at imaginary μ with analytic continuation. In the analytic continuation, we must pay attention to the structure of the phase diagram in the imaginary μ region where QCD has two characteristic properties, the Roberge-Weiss (RW) periodicity and the RW transition [27]. The QCD grand partition function has a periodicity of $2\pi/N_c$ in θ:

$$Z(\theta) = Z\left(\theta + \frac{2\pi k}{N_c}\right) \tag{5}$$

for integer k and the numbers of colors N_c. This periodicity was found by Roberge and Weiss and is now called RW periodicity. Roberge and Weiss also showed that a first-order phase transition occurs at $T > T_{RW}$ and $\theta = (2k+1)\pi/N_c$. This transition is named the RW transition, and T_{RW} is slightly larger than the pseudocritical temperature T_{c0} of the deconfinement transition at zero μ. These features are remnants of Z_{N_c} symmetry in the pure gauge limit. These properties are confirmed by LQCD simulations [4–10,25,26].

The RW periodicity does not mean that Z_{N_c} symmetry is exact. Hence, there is no *a priori* reason that the order parameter for Z_{N_c} symmetry such as the Polyakov loop Φ is zero in the confinement phase. In fact, in the case of $N_c = 3$, the Polyakov loop is always finite even in the confinement phase, when T is finite. However, the case of $N_c = 2$ is special [25]. In this case, the action and the boundary conditions are invariant at $\mu_I/T = (2k+1)\pi/2$ under the CZ_2 transformation composed of the Z_2 transformation and charge conjugation C [28]. Because of this symmetry, the Polyakov loop becomes zero at low T when $\mu_I/T = (2k+1)\pi/2$. Paying attention to these characteristic features, Cea *et al.* [25,26] analyzed the validity of analytic continuation in QC_2D and found that lattice QC_2D (LQC_2D) data at real μ can be described by a suitable analytic function, when the coefficients of the analytic function are determined from LQC_2D data at imaginary μ.

The results of LQCD at imaginary μ are also useful for determining the parameters of effective models, such as the Polyakov-loop extended Nambu–Jona-Lasinio (PNJL) model [29–35]. Here we call this approach the "imaginary chemical potential matching approach" [36]. It is known that the PNJL model can reproduce the results of LQCD at imaginary μ, at least qualitatively, since the model has the RW periodicity and the RW transition [37,38]. It was proposed [39] that the strength G_v of the vector-type four-quark interaction [40,41], which is expected to be important for the physics of neutron stars, may be determined from LQCD data at imaginary μ; for the relation between neutron star properties and G_v, see Ref. [42] and references therein. In Refs. [43] and [44], in fact, G_v is determined with this prescription. The validity of such a determination of parameters in effective models can be checked in QC_2D.

In this paper, we study the phase structure of QC_2D at both real and imaginary μ by performing simulations on an $8^3 \times 4$ lattice with the renormalization-group-improved Iwasaki gauge action [45,46] and the clover-improved two-flavor Wilson fermion action [47] and by analyzing the QC_2D data with the PNJL model. We first test the analytic continuation from imaginary μ to real μ by comparing LQC_2D data calculated at real μ with the results of an analytic function, the coefficients of which are determined from LQC_2D data at imaginary μ. Such a test was carried out in Refs. [25,26] with staggered fermions. Here the test is made with clover-improved Wilson fermions by assuming a polynomial series in the deconfinement phase and a Fourier series in the confinement phase.

We also test the validity of the PNJL model by comparing LQC_2D results with model ones. The PNJL model is good in the deconfinement region, but less accurate in the confinement region. This problem is cured by introducing the baryon degree of freedom to the model. It is also found that the vector-type four-quark interaction is necessary to explain QC_2D data on the quark number density n_q.

This paper is organized as follows. Section II presents the lattice action and the parameter setting used in our LQC_2D simulations. The definition of physical quantities is also presented. In Sec. III, the PNJL model is recapitulated. In Sec. IV, numerical results of LQC_2D are shown and the analytical continuation of physical quantities from imaginary μ to real μ is tested. A comparison between LQC_2D data and PNJL results is made in Sec. V. Errors and uncertainties in the fitting of parameters of the PNJL model are also discussed. Section VI is devoted to a summary.

II. LATTICE SIMULATIONS

A. Lattice action

We use the renormalization-group-improved Iwasaki gauge action S_G [45,46] and the clover-improved two-flavor Wilson quark action S_Q [47] defined by

$$S = S_G + S_Q, \tag{6}$$

$$S_G = -\beta \sum_x \left(c_0 \sum_{\mu<\nu;\mu,\nu=1}^{4} W_{\mu\nu}^{1\times 1}(x) + c_1 \sum_{\mu\neq\nu;\mu,\nu=1}^{4} W_{\mu\nu}^{1\times 2}(x) \right), \tag{7}$$

$$S_{\mathrm{Q}} = \sum_{f=u,d} \sum_{x,y} \bar{q}_x^f M_{x,y} q_y^f, \tag{8}$$

where q is the quark field, $\beta = 4/g^2$, $c_1 = -0.331$, $c_0 = 1 - 8c_1$, and

$$\begin{aligned} M_{x,y} = \delta_{xy} &- \kappa \sum_{i=1}^{3} \{(1-\gamma_i) U_{x,i} \delta_{x+\hat{i},y} + (1+\gamma_i) U_{y,i}^{\dagger} \delta_{x,y+\hat{i}}\} \\ &- \kappa \{e^{\mu}(1-\gamma_4) U_{x,4} \delta_{x+\hat{4},y} + e^{-\mu}(1+\gamma_4) U_{y,4}^{\dagger} \delta_{x,y+\hat{4}}\} \\ &- \delta_{xy} c_{\mathrm{sw}} \kappa \sum_{\mu<\nu} \sigma_{\mu\nu} F_{\mu\nu}. \end{aligned} \tag{9}$$

Here κ is the hopping parameter, $F_{\mu\nu}$ is the lattice field strength, and $F_{\mu\nu} = (f_{\mu\nu} - f_{\mu\nu}^{\dagger})/(8i)$, with $f_{\mu\nu}$ the standard clover-shaped combination of gauge links.

We apply the CP-PACS parametrization scheme [48] for determining the coefficient c_{sw} of the clover term in the two-color case. The coefficient c_{sw} is determined by using a result obtained in a perturbative mean-field-improved value $c_{\mathrm{sw}} = P^{-3/4}$ [49] with the plaquette P calculated in one-loop perturbation theory, $P = 1 - 0.21027 \frac{N_c^2-1}{2} \beta^{-1}$ for $N_c = 2$ [50]. We also check that the one-loop value of P reproduces the measured ones in the simulations within 10%.

In this paper, we deal with only the region $\mu \ll m_{\mathrm{ps}}/2 \sim 308$ MeV, where m_{ps} is the pseudoscalar (PS) meson mass. In NJL-like effective models such as the PNJL model, the diquark condensate appears only when $\mu > m_{\mathrm{ps}}/2$. We then assume that no diquark condensate comes out in the present analysis and do not add any diquark source term to the lattice action to see whether the diquark condensate appears in our lattice simulations.

B. Parameter setting for simulations

We denote temporal and spatial lattice sizes as N_t and N_s, respectively. The hybrid Monte Carlo algorithm is used to generate full $\mathrm{QC_2D}$ configurations with two-flavor dynamical quarks. The simulations are performed on a lattice of $N_s^3 \times N_t = 8^3 \times 4$. The step size of molecular dynamics is $\delta\tau = 0.02$ and the step number of the dynamics is $N_\tau = 50$. The acceptance ratio is more than 95%. We generated 10,000 trajectories and removed the first 5,000 trajectories as thermalization for the entire parameter set. The relation of parameters κ and β to the corresponding T/T_{c0} is determined by finding the line of constant physics where the ratio of the pseudoscalar meson mass m_{ps} to the vector meson mass m_{v} at $T = \mu = 0$ is invariant; see Table I for the relation.

To obtain the results in Table I, we calculated the pseudoscalar meson mass m_{ps} and vector meson mass m_{v} in vacuum on an $N_s^3 \times N_t = 8^3 \times 16$ lattice when $\beta = 0.6,\ 0.64,\ 0.66,\ 0.68,\ 0.70,\ 0.72,\ 0.74,\ 0.76,$ and 0.78. Using the data, we determined the relation among β, κ, and lattice spacing a, imposing the relation $m_{\mathrm{ps}}/m_{\mathrm{v}} \sim 0.8$ and $m_{\mathrm{v}} = 770$ MeV. The corresponding temperature T in the smaller lattice is obtained by using the relation $T = 1/(N_t a)$. For $\beta = 0.65$ and 0.75, we have determined the β-κ-T relation by interpolation. We have determined the critical beta β_{c0} at $\mu = 0$ by measuring the susceptibility of the Polyakov loop and the pseudocritical temperature T_{c0} by using the β-T relation obtained by the interpolation.

TABLE I. Summary of the simulation parameter in this paper. T_{c0} is the pseudocritical temperature at $\mu = 0$. In this parameter setting, except for $\beta = 0.65$ and 0.75, the lattice spacing a is about $1.38218 \sim 1.95711$ [GeV^{-1}] and the ratio $m_{\mathrm{p}}/m_{\mathrm{v}} = 0.8$ at $T = 0$. For $\beta = 0.65$ and 0.75, we have determined the β-κ-T relation by interpolation.

N_s	N_t	β	κ	T/T_{c0}
8	4	0.60000	0.13782	0.87783(585)
		0.64000	0.13770	0.94126(628)
		0.65000	0.13764	0.96229(645)
		0.66000	0.13751	0.98577(657)
		0.68000	0.13695	1.02608(84)
		0.70000	0.13677	1.06282(709)
		0.72000	0.13679	1.11629(745)
		0.74000	0.13567	1.16526(77)
		0.75000	0.13526	1.18160(792)
		0.76000	0.13493	1.20197(802)
		0.78000	0.13443	1.24298(829)

C. Physical observables

In this paper, we calculate the Polyakov loop (Φ), the quark number density (n_q), and the chiral condensate (σ). The quark number density is calculated by

$$n_q = \frac{T}{V} \frac{\partial}{\partial \mu} \log Z, \tag{10}$$

where V is the spatial volume, and σ is by

$$\sigma = \langle \bar{q} q \rangle, \tag{11}$$

where q is quark field and the $\langle O \rangle$ is the average value of physical quantity O. The chiral condensate suffers from the renormalization, and chiral symmetry is explicitly broken by Wilson fermions. This makes it difficult to deal with the absolute value of the chiral condensate itself. We then consider a variation

$$\delta\sigma(T,\mu) = \sigma(T,\mu) - \sigma(T,0). \tag{12}$$

The Polyakov-loop operator is defined by

$$L(\boldsymbol{x}) = \frac{1}{N_c} \prod_{t=1}^{N_t} U_4(\boldsymbol{x}, t), \tag{13}$$

with link variables $U_\mu \in \mathrm{SU}(2)$. The average value Φ of L is related to the single static-quark free energy F_q as

$$\Phi = \langle L \rangle \sim e^{-F_q/T}. \tag{14}$$

The Polyakov loop Φ is an order parameter of the confinement/deconfinement transition if quark mass m is infinitely large. In fact, if F_q is finite (infinite), Φ is finite (zero). The symmetry associated with the confinement/deconfinement transition is Z_2 symmetry under the transformation

$$U_4(\mathbf{x}, t) \to z_2(t) U_4(\mathbf{x}, t), \tag{15}$$

where z_2 is the element of the Z_2 group that depends only on the temporal coordinate t. Pure gauge action is invariant under this transformation while L is not. Hence, $\Phi = \langle L \rangle$ is an order parameter of Z_2 symmetry breaking. Effects of dynamical quarks break Z_2 symmetry explicitly and Φ is not a proper order parameter of the confinement/deconfinement transition. As mentioned in the previous section, however, at $\theta = (2k+1)\pi/2$ the system is symmetric under the $\mathcal{C}Z_2$ transformation [28]. Hence, Φ becomes an order parameter of the combined symmetry there.

III. PNJL MODEL

Two-color QCD has Pauli-Gürsey symmetry in the limit of $m = \mu = 0$ [51,52]. The PNJL Lagrangian of $\mathrm{QC_2D}$ is so constructed as to have the symmetry and is given by [28,53,54]

$$\begin{aligned}\mathcal{L} = {} & \bar{q}(i\gamma^\nu D_\nu - m)q \\ & + G[(\bar{q}q)^2 + (\bar{q} i\gamma_5 \vec{\tau} q)^2 + |q^T C i\gamma_5 \tau_2 t_2 q|^2] \\ & + G_8[(\bar{q}q)^2 + (\bar{q} i\gamma_5 \vec{\tau} q)^2 + |q^T C i\gamma_5 \tau_2 t_2 q|^2]^2 \\ & - G_\mathrm{v}(\bar{q}\gamma^\nu q)^2 - \mathcal{U}(\Phi),\end{aligned} \tag{16}$$

where q, m, t_i, τ_i, G, G_8, G_v are the two-flavor quark fields, the current quark mass, the Pauli matrices in the color and flavor spaces, the coupling constants of the scalar-type four-quark interaction, the scalar-type eight-quark interaction, and the vector-type four-quark interaction, respectively. The potential $\mathcal{U}$ is a function of Φ.

The mean-field approximation leads us to the thermodynamical potential Ω as [53]

$$\begin{aligned}\Omega = {} & -2N_f \int \frac{d^3p}{(2\pi)^3} \sum_\pm [E_p^+ + E_p^- + T(\ln f^- + \ln f^+)] \\ & + U + \mathcal{U}(\Phi),\end{aligned} \tag{17}$$

with

$$f^\pm = 1 + 2\Phi e^{-\beta E_p^\pm} + e^{-2\beta E_p^\pm}, \tag{18}$$

$$U = G(\sigma^2 + \tilde{\Delta}^2) + 3G_8(\sigma^2 + \tilde{\Delta}^2)^2 - G_\mathrm{v} n_q^2, \tag{19}$$

where N_f is the number of flavors, and $\tilde{\Delta} = |\langle q^T C i\gamma_5 \tau_2 t_2 q \rangle|$ is the diquark condensate. The $E_p^\pm$ are defined by

$$E_p^\pm = \mathrm{sgn}(E_p \pm \tilde{\mu}) \sqrt{(E_p \pm \tilde{\mu})^2 + \Delta^2}, \tag{20}$$

where $E_p \equiv \sqrt{p^2 + M^2}$ with the effective quark mass $M \equiv m - 2G\sigma - 4G_8\sigma(\sigma^2 + \tilde{\Delta}^2)$, $\tilde{\mu} = \mu - 2G_\mathrm{v} n_q$, $\Delta = -2G\tilde{\Delta}$, and $\mathrm{sgn}(E_p \pm \tilde{\mu})$ is the sign function. When $m = \mu = 0$, Ω becomes invariant under the rotation in the σ-$\tilde{\Delta}$ plane as a consequence of Pauli-Gürsey symmetry. Usually, G is assumed to be constant. However, they may depend on Φ [55]. Here we consider Φ-dependent G, namely,

$$G \equiv G_0(1 - \alpha\Phi^2), \tag{21}$$

where G_0 and α are constant parameters. As usual, we assume that G_8 is constant.

In the Polyakov gauge, Φ is given by

$$\Phi = \frac{1}{2}(e^{i\phi} + e^{-i\phi}) = \cos(\phi), \tag{22}$$

for real number ϕ. Following Ref. [53], we take the Polyakov-loop effective potential of the form

$$\frac{\mathcal{U}(\Phi)}{T} = -b[24e^{-a/T}\Phi^2 + \ln(1 - \Phi^2)], \tag{23}$$

where a and b are constant parameters. As will be mentioned in the next section, we determine the three parameters α, a, and b, to reproduce $\mathrm{LQC_2D}$ data on n_q at $\beta = 0.75$ in the imaginary chemical potential region and reproduce the pseudocritical temperature $T_{c0} = 146$ MeV at $\mu = 0$. The obtained values are $\alpha = 0.2$, $a = 300$ MeV, and $b^{1/3} = 100$ MeV.

Because this model is nonrenormalizable, the first two terms in the integral of Ω are divergent. We then regularize them by introducing a three-dimensional momentum cutoff as

$$\int \frac{d^3p}{(2\pi)^3} \to \frac{1}{2\pi^2} \int_0^\Lambda dp\, p^2. \tag{24}$$

The mean fields $X = \sigma$, Δ, n_q, Φ are determined from the stationary conditions

$$\frac{\partial \Omega}{\partial X} = 0. \tag{25}$$

In this paper, we consider only the region $\mu \ll m_\mathrm{ps}/2 \sim$ 308 MeV. In NJL-like effective models such as the PNJL model, it is known that the diquark condensate appears only when $\mu > m_\mathrm{ps}/2$. In fact, we confirmed that Δ is zero there, using the PNJL model. This fact is consistent with our assumption that the diquark condensate does not appear also in our LQCD calculation.

There are six parameters in the NJL sector of the PNJL model. A standard parameter set is already known for the

TABLE II. Parameters of the PNJL model. The parameters reproduce $m_{\rm ps} = 616$ MeV. M_0 is the effective quark mass in vacuum obtained in the PNJL model.

$m_{\rm ps}$ (MeV)	M_0 (MeV)	G_0 (GeV^{-2})	G_8 (GeV^{-8})
616	354	4.6	60
$G_{\rm v}/G_0$	Λ [MeV]	m [MeV]	α
0.15	700	110	0.2
a [MeV]	$b^{1/3}$ [MeV]		
300	100		

two-color PNJL model with light pseudoscalar meson mass ($m_{\rm ps} = 140$ MeV) [53]. In the standard parameter set, $\Lambda = 657$ MeV is used. In our case, since $m_{\rm ps}$ is larger, we adopt a somewhat larger value, $\Lambda = 700$ MeV. We also require the effective quark mass M_0 to be considerably smaller than Λ and larger than half of the pseudoscalar meson mass $m_{\rm ps}$. The latter is the condition for the meson to be the Nambu-Goldstone boson. We search the parameter set of G_0, G_8, and m, which reproduce the lattice $m_{\rm ps}$ value ($\sim$616 MeV), under the conditions above. The values of $G_{\rm v}$ and α are chosen to reproduce LQC$_2$D data on n_q; see Sec. V. Table II shows the parameter set used in this paper.

IV. ANALYTICAL CONTINUATION OF PHYSICAL QUANTITIES

A. Analytical continuation

In this section, we show the numerical results of LQC$_2$D simulations and perform the analytical continuation of physical quantities from the region at imaginary μ to the region at real μ, and finally examine the validity of analytical continuation.

Figure 1 shows the T dependence of Φ for several values of $\hat{\mu} \equiv \mu/T$ from $i\pi/2$ to 1.2. For all the cases except

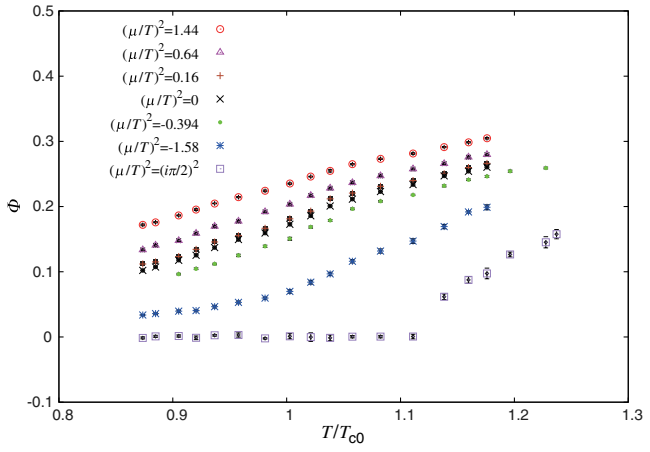

FIG. 1. LQC$_2$D results on T dependence of Φ for several values of $\hat{\mu}^2 = (\mu/T)^2$.

$\hat{\mu}^2 = (i\pi/2)^2 = -(\pi/2)^2$, Φ increases smoothly as T goes up. The deconfinement transition is thus crossover there. This property is the same as in QCD with three colors [56]. For each $\hat{\mu}^2$, the pseudocritical temperature $T_c(\hat{\mu}^2)$ [or $\beta_c(\hat{\mu}^2)$] is defined by the temperature where the susceptibility of Φ becomes maximum. It is found from LQC$_2$D simulations at $\hat{\mu} = 0$ that $T_{c0} \equiv T_c(0) = 146$ MeV. As for $\hat{\mu}^2 = (i\pi/2)^2$, Φ is almost zero below $T = 1.12T_{c0}$ and increases rapidly above $T = 1.14T_{c0}$. At $\hat{\mu} = i\theta = i\pi/2$, as mentioned in Sec. I, the system has $\mathcal{C}Z_2$ symmetry and hence the order parameter Φ of $\mathcal{C}Z_2$ symmetry is zero below $T_{\rm RW}$ and finite above $T_{\rm RW}$. Therefore, we can roughly estimate that $T_{\rm RW}$ is located somewhere in the range of $T = 1.1 \sim 1.2T_{c0}$, although it is not clear from the present analysis whether the RW transition is a first-order or second-order phase transition on the RW end point.

Figure 2 shows the pseudocritical line $\beta_c(\hat{\mu}^2)$ in the $\hat{\mu}^2$-β plane, and it is found that $\beta_c(\hat{\mu}^2)$ decreases as $\hat{\mu}^2$ increases. The value of $T_c(\hat{\mu}^2)$ at $\hat{\mu}^2 = (i\pi/2)^2$ determined from $\beta_c((i\pi/2)^2)$ is $1.16T_{c0}$. This value is a better value for $T_{\rm RW}$ than the one obtained by using Fig. 1.

Now we test the analytic continuation from imaginary μ to real μ for the cases of $\beta = 0.75$, 0.70, 0.65, and 0.60 that correspond to $T/T_{c0} = 1.18$, 1.06, 0.96, and 0.88, respectively. The system is in the deconfinement (D) phase at $\beta = 0.75$, while it is in the confinement (C) phase at $\beta = 0.60$ in the entire range of μ^2 that we have studied. At $\beta = 0.70(0.65)$, the system is in the C-phase when $\hat{\mu}^2 < -1.15(1.35)$ and in the D-phase when $\hat{\mu}^2 > -1.15(1.35)$. For each temperature, we then use different analytic functions as explained below [25,26,57].

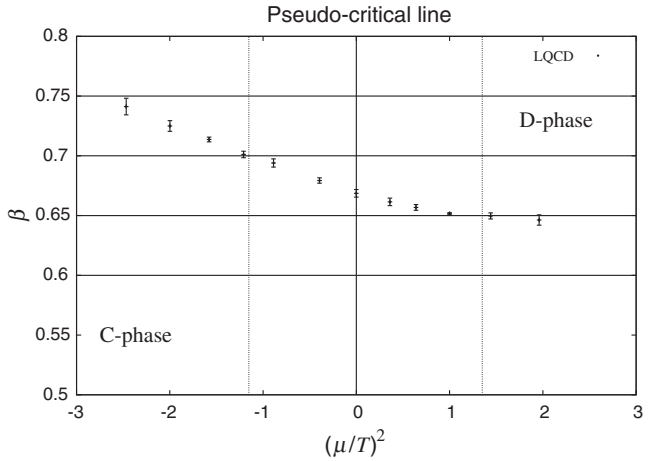

FIG. 2. Pseudocritical line of deconfinement transition in the $\hat{\mu}^2$-β plane. In each thin horizontal solid line, β is constant, and in each thin vertical dotted line $\hat{\mu}^2$ is constant. At $\beta = 0.70$, the left-hand side of the left thin vertical dotted line belongs to the C-phase, and the right side to the D-phase. At $\beta = 0.65$, the left-hand side of the right thin vertical dotted line corresponds to the C-phase, and the right side to the D-phase. Note that $\beta_c(0) = 0.67$.

1. $T_{\mathrm{RW}} < T(\beta = 0.75)$

At this temperature, due to the existence of the RW transition, physical quantities cannot be described by any continuous periodic function. Hence we use a polynomial series of the form

$$A + B\hat{\mu}^2, \tag{26}$$

or

$$A + B\hat{\mu}^2 + C\hat{\mu}^4, \tag{27}$$

for $\hat{\mu}$-even quantities Φ and σ, where A, B, C are expansion coefficients. For a $\hat{\mu}$-odd quantity n_q, we use

$$A\hat{\mu} + B\hat{\mu}^3, \tag{28}$$

or

$$A\hat{\mu} + B\hat{\mu}^3 + C\hat{\mu}^5. \tag{29}$$

In Ref. [25], it is discussed that better results are obtained using ratios of polynomials (Padé approximations). It would be interesting to examine the approximations in our future works.

2. $T_{c0} < T(\beta = 0.70) < T_{\mathrm{RW}}$

At this temperature, the system is in the D-phase when $\hat{\mu}^2 > -1.15$. We then use the same polynomial series as in the case of $\beta = 0.75$, but consider only the region $-1.15 < \hat{\mu}^2 \leq 0$ as a fitting range. For Φ and σ, we use only the quadratic function (26), since the number of data we can use is small.

3. $T(\beta = 0.60, 0.65) < T_{c0}$

At this temperature, the system is in the C-phase at imaginary and zero $\hat{\mu}$. Hence, it is expected that physical quantities can be well described by continuous periodic functions. Since $\Phi(\theta)$ is θ-even and has a periodicity of 2π in $\theta = \mathrm{Im}(\hat{\mu})$, we use the following Fourier series,

$$A\cos(\theta), \tag{30}$$

or

$$A\cos(\theta) + B\cos(3\theta), \tag{31}$$

for Φ. Note that the terms of $\cos(2\theta)$ and $\cos(4\theta)$ as well as the constant term are excluded, since $\Phi(\pi/2 + \theta') = -\Phi(\pi/2 - \theta')$ for any θ'. The chiral condensate $\sigma(\theta)$ is a θ-even and periodic function with a period π. We then use the following Fourier series,

$$A + B\cos(2\theta), \tag{32}$$

or

$$A + B\cos(2\theta) + C\cos(4\theta), \tag{33}$$

for σ. The quark number density $n_q(\theta)$ is a θ-odd and periodic function with a period π. We therefore use the following Fourier series,

$$A\sin(2\theta), \tag{34}$$

or

$$A\sin(2\theta) + B\sin(4\theta), \tag{35}$$

for n_q. Note that, in the case of $\beta = 0.65$, the system is in the D-phase when $\hat{\mu}^2 > 1.35$. Hence, the Fourier series in which the coefficients are determined from LQCD data at imaginary $\hat{\mu}$ and zero $\hat{\mu} = 0$ may not work there.

4. Pseudocritical line

The pseudocritical line $\beta_c(\hat{\mu}^2)$ is $\hat{\mu}$-even. We then use the polynomial series (26) and (27).

B. Quark number density

First we consider the analytic continuation of n_q. Figure 3 shows the $\hat{\mu}^2$ dependence of $(n_q/T^3)^2$ for several values of T. The analytic continuation has errors coming from LQCD data at zero and imaginary $\hat{\mu}$. We then plot the upper and lower bounds of analytic continuation with a pair of the same lines. The $(n_q/T^3)^2$ are smooth at $\hat{\mu} = 0$, as expected. This is true for $\delta\sigma$ and Φ, as shown later. This guarantees that the analytic continuation from imaginary $\hat{\mu}$ to real $\hat{\mu}$ is possible.

At $\beta = 0.75$ $(T/T_{c0} = 1.18)$, the system is in the D-phase and hence the polynomial series is used. The coefficients determined from LQCD data at imaginary μ are tabulated in Table III. The polynomial series up to $\hat{\mu}^3$ reproduces $\mathrm{LQC_2D}$ data well in the wide range of $0 \leq \hat{\mu}^2 \leq (1.2)^2$. Note that the analytic function deviates from $\mathrm{LQC_2D}$ data near the first-order RW phase transition present at $T > T_{\mathrm{RW}}$ and $\hat{\mu}^2 = -(\pi/2)^2$.

At $\beta = 0.70$ $(T/T_{c0} = 1.06)$, the system is in the C-phase when $\hat{\mu}^2 < -1.15$, while it is in the D-phase otherwise. Hence, we use only seven data in the range of $\hat{\mu}^2 = -1.15 \sim 0$ to determine the coefficients of the polynomial series. The coefficients of the function are tabulated in Table III. $\mathrm{LQC_2D}$ data calculated at real $\hat{\mu}$ lie between the upper and lower bounds of the polynomial series up to $\hat{\mu}^3$ in the wide range of $0 \leq \hat{\mu}^2 \leq (1.2)^2$.

At $\beta = 0.65$ $(T/T_{c0} = 0.96)$, the system is in the C-phase when $\hat{\mu}^2 < 1.35$, while it is in the D-phase otherwise. Hence, we use the Fourier series. The coefficients of the function are tabulated in Table III. The analytic functions fail to reproduce $\mathrm{LQC_2D}$ data calculated at real $\hat{\mu}$ when $\hat{\mu}^2 \geq 0.4$. The large deviation at large $\hat{\mu}^2$ may originate in the fact that the system is in the D-phase there and the Fourier series may not be valid anymore.

At $\beta = 0.60$ $(T/T_{c0} = 0.88)$, the system is in the C-phase. Therefore, we use the Fourier series. The coefficients of the function are tabulated in Table III. The Fourier series up to the term $\sin(2\theta)$ $[\sin(4\theta)]$ are consistent with $\mathrm{LQC_2D}$ data calculated at real $\hat{\mu}$ in the wide range $0 \leq \hat{\mu}^2 < 0.8$ $[0 \leq \hat{\mu}^2 \leq (1.2)^2]$.

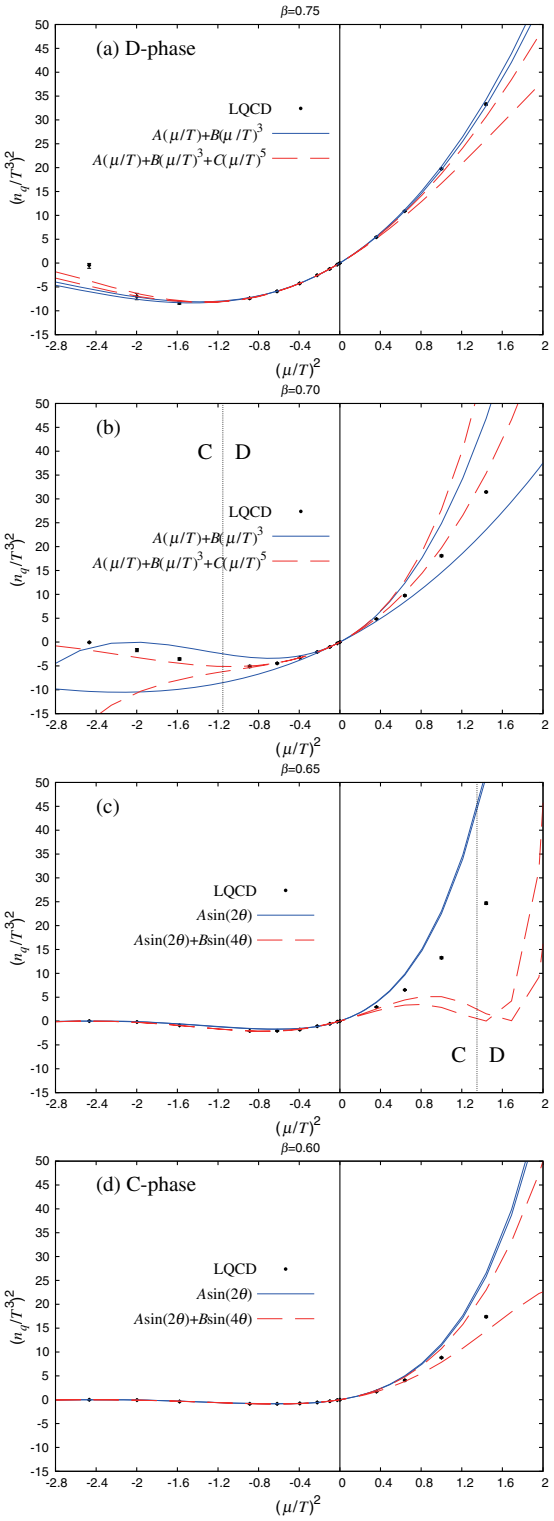

FIG. 3. $\hat{\mu}^2$ dependence of n_q at (a) $\beta = 0.75$ $(T/T_{c0} = 1.18)$, (b) $\beta = 0.70$ $(T/T_{c0} = 1.06)$, (c) $\beta = 0.65$ $(T/T_{c0} = 0.96)$, and (d) $\beta = 0.60$ $(T/T_{c0} = 0.88)$. The dots with error bars are the results of LQC_2D data. The solid and dashed lines represent the results of analytic continuation in which two types of analytic functions are taken as shown by legends. The upper and lower bounds of analytic continuation are shown by a pair of same lines. Characters C and D denote confinement and deconfinement phases, respectively.

Comparing four cases of T/T_{c0} with one another, one can see that the analytic continuation is reasonable at higher T/T_{c0} where the system is always in the D-phase when $\hat{\mu}^2$ varies from $-(\pi/2)^2$ to $(1.2)^2$ and at lower T/T_{c0} where the system is always in the C-phase when $\hat{\mu}^2$ varies from $-(\pi/2)^2$ to $(1.2)^2$. Near $T/T_{c0} = 1$, however, the system changes from the C-phase to the D-phase as $\hat{\mu}^2$ varies from $-(\pi/2)^2$ to a positive value. A simple analytic function cannot follow the complicated change properly. Therefore, the analytic continuation is reasonable except for the vicinity of deconfinement crossover.

C. Chiral condensate

Figure 4 shows the $\hat{\mu}^2$ dependence of $\delta\sigma$ for several values of T. Again, the upper and lower bounds of analytic continuation are shown by a pair of lines of the same kind; see Table III for the coefficients of the analytic function determined from LQC_2D data at imaginary μ. As for $\delta\sigma$, one can make the same discussion as in Sec. IV B for n_q, as shown below, although the analytic function taken in the C-phase is a cosine function.

At $\beta = 0.75$ $(T/T_{c0} = 1.18)$, the polynomial series up to $\hat{\mu}^2$ reproduces well the LQC_2D data calculated at real $\hat{\mu}$ in the wide range of $0 \le \hat{\mu}^2 \le (1.2)^2$. At $\beta = 0.70$ $(T/T_{c0} = 1.06)$, the system is in the C-phase when $\hat{\mu}^2 < -1.15$, while it is in the D-phase otherwise. Hence, we can use only three data in the range of $\hat{\mu}^2 = -1.15 \sim 0$ to determine the coefficients of the analytic function and then use the quadratic function only. The function is consistent with LQC_2D calculated at real $\hat{\mu}$ in the wide range of $0 \le \hat{\mu}^2 \le (1.2)^2$.

At $\beta = 0.65$ $(T/T_{c0} = 0.96)$, the system is in the C-phase when $\hat{\mu}^2 < 1.35$, while it is in the D-phase otherwise. Hence, we use the Fourier series. The analytic function is not consistent with LQC_2D data calculated at real $\hat{\mu}$ when $\hat{\mu}^2 > 0.4$. As mentioned in the case of n_q, this failure at large $\hat{\mu}$ may show that the system is in the D-phase there and the Fourier series becomes less reliable. At $\beta = 0.60$ $(T/T_{c0} = 0.88)$, the system is in the C-phase. Hence, we use the Fourier series. The analytic functions are consistent with LQC_2D data calculated at real $\hat{\mu}$ in the range of $0 \le \hat{\mu}^2 < 0.8$.

D. Polyakov loop

Figure 5 shows the $\hat{\mu}^2$ dependence of Φ at several values of T. Again, the upper and lower bounds of analytic continuation are shown by a pair of same lines; see Table III for the coefficients of the analytic function. As for Φ, one can make the same discussion qualitatively as in Sec. IV C for $\delta\sigma$.

E. Pseudocritical line

Figure 6 shows the transition line of deconfinement crossover in the $\hat{\mu}^2$-β plane. The pseudocritical $\beta_c(\hat{\mu}^2)$ at $\hat{\mu}^2 = 0$ is about 0.67. We consider the polynomial series in

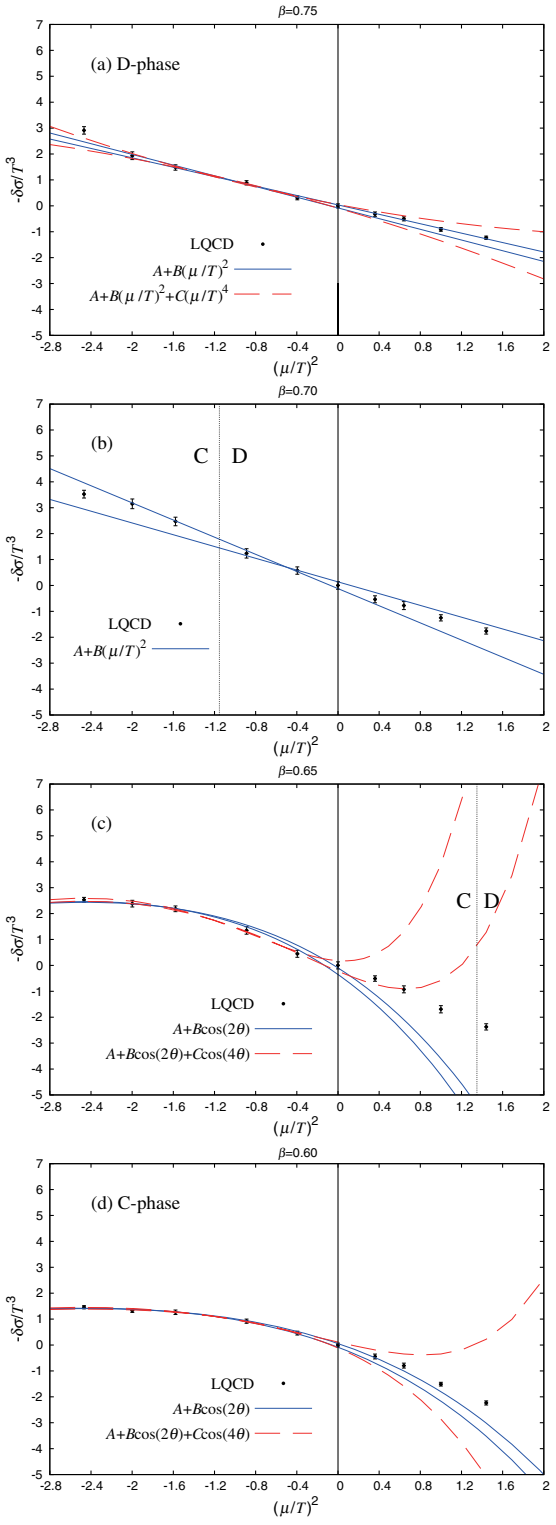

FIG. 4. $\hat{\mu}^2$ dependence of σ at (a) $\beta = 0.75$ $(T/T_{c0} = 1.18)$, (b) $\beta = 0.70$ $(T/T_{c0} = 1.06)$, (c) $\beta = 0.65$ $(T/T_{c0} = 0.96)$, (d) $\beta = 0.60$ $(T/T_{c0} = 0.88)$. For the definition of dots, lines, and characters, see the Fig. 3 caption.

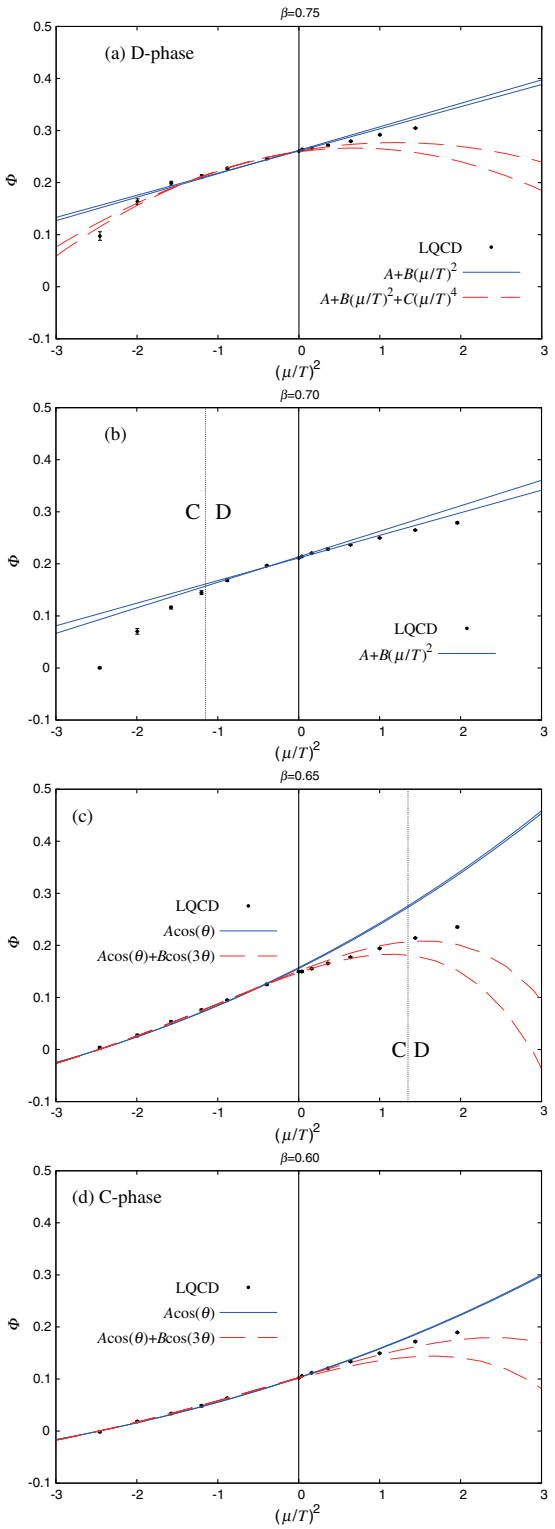

FIG. 5. $\hat{\mu}^2$ dependence of Φ at (a) $\beta = 0.75$ $(T/T_{c0} = 1.18)$, (b) $\beta = 0.70$ $(T/T_{c0} = 1.06)$, (c) $\beta = 0.65$ $(T/T_{c0} = 0.96)$, and (d) $\beta = 0.60$ $(T/T_{c0} = 0.88)$. For the definition of dots, lines, and characters, see the Fig. 3 caption.

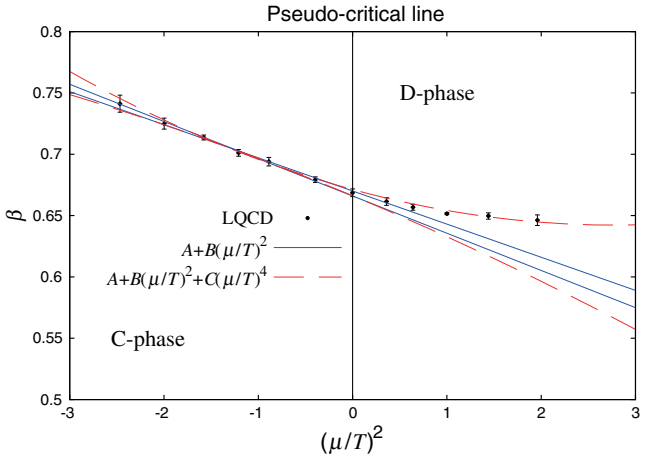

FIG. 6. Pseudocritical line of deconfinement crossover in the $\hat{\mu}^2$-β plane. Note that $\beta_c(0) = 0.67$. For the definition of dots, lines, and characters, see the Fig. 3 caption.

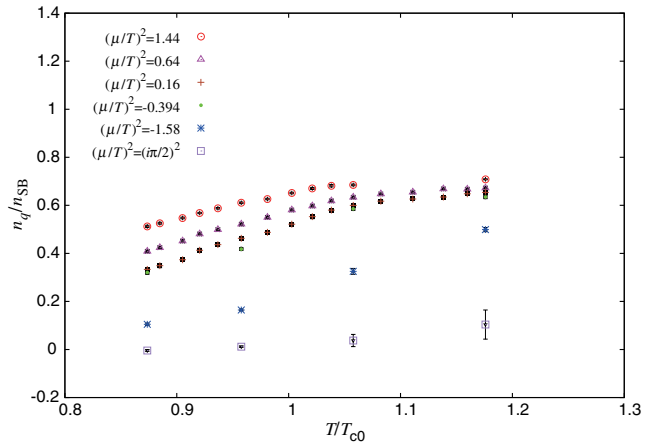

FIG. 7. T dependence of $n_q/n_{\rm SB}$ for several values of $\hat{\mu}^2$. Six cases of $\hat{\mu}^2 = (i\frac{\pi}{2})^2$, -1.58, -0.394, 0.16, 0.64, 1.44 are shown from the bottom. In this paper, $n_{\rm SB}$ in the same size lattice is used to divide the lattice results [11].

which the coefficients are obtained from LQC$_2$D data at imaginary μ and tabulated in Table IV. The polynomial series up to $\hat{\mu}^2$ reproduces the LQC$_2$D data well at $0 \le \hat{\mu}^2 < 0.8$, but deviates at $\hat{\mu}^2 > 0.8$. The polynomial series up to $\hat{\mu}^4$ is consistent with LQC$_2$D data even at $\hat{\mu}^2 > 0.8$, but the difference between the upper and lower bounds of analytic continuation is large. Therefore, we should consider that the analytic continuation of the pseudocritical line is reasonable at $0 \le \hat{\mu}^2 < 0.8$.

V. COMPARISON OF PNJL MODEL WITH LQC$_2$D DATA

A. Parameter setting

In this section, we compare the results of the PNJL model with LQC$_2$D data to test the validity of the model. For this purpose, we first fix the parameters of the model. For the NJL sector, except for $G_{\rm v}$, the parameters have already been determined in Sec. III. We then fix the remaining parameters a, b, α, and $G_{\rm v}$ here.

Figure 7 shows the T dependence of n_q divided by its Stephan-Boltzmann (SB) limit $n_{\rm SB}$ for several values of $\hat{\mu}^2$ from $-(\pi/2)^2$ to $(1.2)^2$. LQC$_2$D results include a lattice artifact due to finite volume and spacing. The artifact is expected to be reduced in $n_q/n_{\rm SB}$. For all the values of $\hat{\mu}^2$, the ratio $n_q/n_{\rm SB}$ increases as T increases.

Now we determine the parameters a, b, α, and $G_{\rm v}$ from n_q at the highest T in the present analyses, i.e., at $\beta = 0.75$ ($T/T_{c0} = 1.18$). The reason why we use the LQCD data at the highest temperature is that the PNJL model is essentially a model for quark dynamics and it is expected to work better at higher T than at lower T. The reason why we use n_q is that the quantity does not need the renormalization and is sensitive to the value of $G_{\rm v}$.

Figure 8 shows the $\hat{\mu}^2$ dependence of $n_q/n_{\rm SB}$ at $\beta = 0.75$ at imaginary μ. As $\hat{\mu}^2$ decreases, the chiral symmetry breaking becomes stronger and the effective quark mass M becomes larger [37], so that $n_q/n_{\rm SB}$ decreases.

We determined parameters a, b, α, and $G_{\rm v}$ in the PNJL model as follows. First, we searched for some parameter sets of (a, b, α) that reproduce $T_{c0} = 146$ MeV. Next, for each parameter set (a, b, α), we searched for the best value of $G_{\rm v}$ that reproduces the $\hat{\mu}^2$ dependence of n_q in Fig. 8 well. Finally, we selected the parameter set $(a, b, \alpha, G_{\rm v})$ that reproduces the results of Fig. 8 best. The parameters thus obtained are shown in Table II. It is interesting that the vector interaction is needed to reproduce LQC$_2$D results data at imaginary μ. In fact, the model with $G_{\rm v} = 0.15G_0$

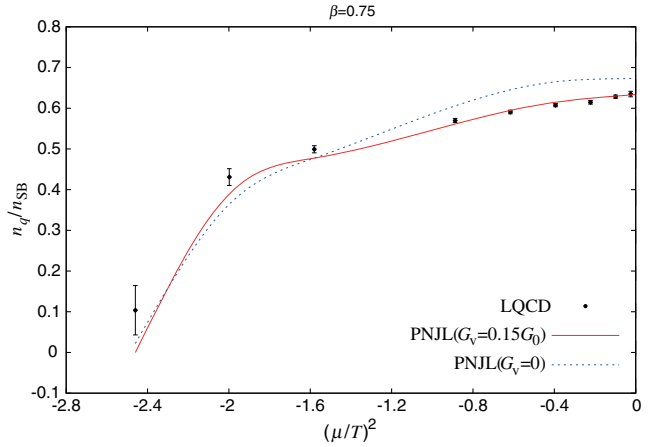

FIG. 8. $\hat{\mu}^2$ dependence of $n_q/n_{\rm SB}$ at $\beta = 0.75$ at imaginary μ. The dots with error bars show the results of LQC$_2$D data. The solid (dotted) line shows the results of the PNJL model with $G_{\rm v}/G_0 = 0.15(0)$. In this paper, $n_{\rm SB}$ in the same size lattice is used to divide the lattice results, while the continuum expression of $n_{\rm SB}$ is used to divide the PNJL results.

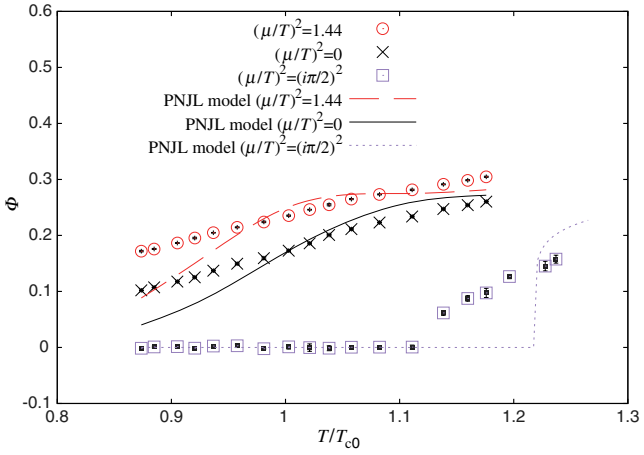

FIG. 9. T dependence of Φ for three values of $\hat{\mu}^2$. The dots represent LQC$_2$D data. The solid (dotted, dashed) line represents the PNJL results at $\hat{\mu}^2 = 0(-(\pi/2)^2, 1.44)$. The PNJL results are multiplied by the normalization factor 0.304.

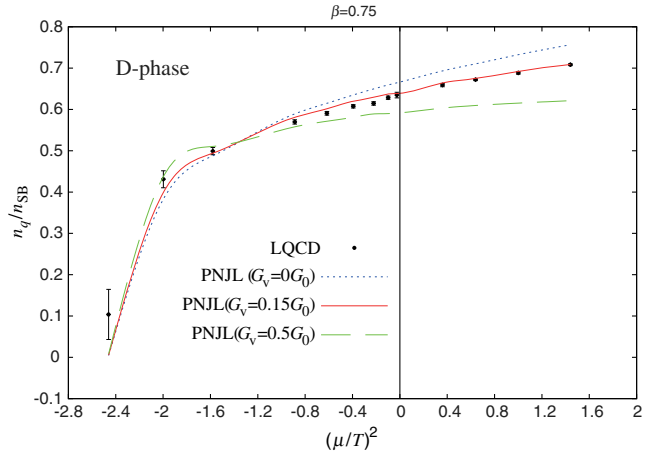

FIG. 10. $\hat{\mu}^2$ dependence of n_q/n_{SB} for $\beta = 0.75$ ($T/T_{c0} = 1.18$). The dots with error bars are the results of LQC$_2$D data, while the solid (dotted) line corresponds to the results of the PNJL model with $G_{\mathrm{v}}/G_0 = 0.15(0, 0.5)$. Note that n_q/n_{SB} at $\hat{\mu} = 0$ is defined by $\lim_{\hat{\mu}\to 0} n_q/n_{\mathrm{SB}}$.

(solid line) yields better agreement with LQC$_2$D data than the model with $G_{\mathrm{v}} = 0$ (dotted line). This method may work as a way of determining the vector coupling also in realistic QCD with three colors [39,43,44].

T dependence of Φ is shown in Fig. 9 for three cases of $\hat{\mu}^2 = -(\pi/2)^2, 0, 1.44$. Since the renormalization is needed for Φ, we multiply the PNJL results by a factor 0.304 to reproduce LQC$_2$D results at $\hat{\mu} = 0$ and $T = T_{c0}$. The renormalized PNJL results (solid lines) reproduce LQC$_2$D data qualitatively, except for the vicinity of the first-order RW phase transition at $T > T_{\mathrm{RW}} \approx 1.16T_{c0}$ and $\hat{\mu}^2 = -(\pi/2)^2$. The value of T_{RW} is 178 MeV in the PNJL model, but $163 \sim 170$ MeV in LQC$_2$D data. In the present model, it is quite difficult to reproduce LQC$_2$D values of T_{c0} and T_{RW} simultaneously. A fine-tuning of the Polyakov potential $\mathcal{U}(\Phi)$ may be necessary.

B. Quark number density

Figure 10 shows the $\hat{\mu}^2$ dependence of n_q/n_{SB} at $\beta = 0.75$ ($T/T_{c0} = 1.18$). As mentioned in the previous subsection, we have used LQC$_2$D on n_q/n_{SB} at $\beta = 0.75$ and imaginary μ to determine the parameter set of the PNJL model. The obtained value of G_{v} is $0.15G_0$. The parameter set thus determined reproduces LQC$_2$D data well even at real μ. This ensures the assumption that the PNJL model is valid at high T. In the same figure, the results obtained by using the PNJL model with $G_{\mathrm{v}}/G_0 = 0$ and 0.5 are also shown. Also note that the PNJL model with $G_{\mathrm{v}}/G_0 = 0$ or 0.5 fails to reproduce LQC$_2$D data at real μ, while the PNJL model with $G_{\mathrm{v}}/G_0 = 0.15$ agrees with the LQC$_2$D data even at real μ. The imaginary chemical potential matching approach is thus a promising method.

Figure 11 shows the same as Fig. 10 but for $\beta = 0.70$ ($T/T_{c0} = 1.06$). On the left (right) side of the vertical thin dotted line, the system is in the C-phase (D-phase). The PNJL result (solid line) underestimates LQC$_2$D data sizably in the C-phase. To improve this, we consider the baryon degrees of freedom that are not taken into account in the PNJL model in the mean-field approximation (MFA); note that baryons (diquark fluctuations) appear only in higher-order calculations beyond MFA. Assuming that the baryons have the same degrees of freedom as PS mesons, we add a contribution of free baryon gas to the n_q calculated with the PNJL model in MFA. It is well known in three-color QCD that the PNJL model in MFA reproduces lattice results well in the confinement phase, when the free baryon (and meson) contribution is added [58].

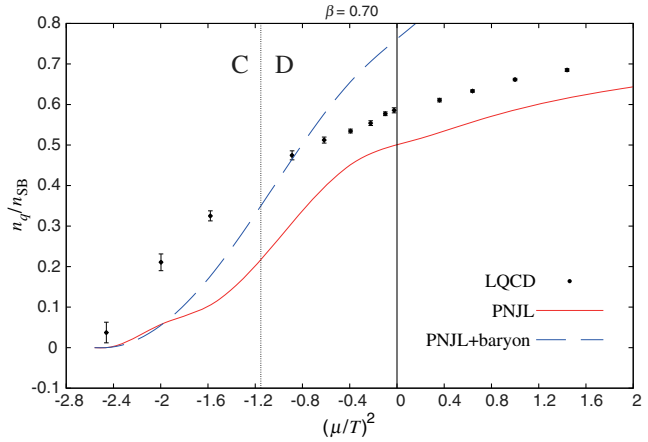

FIG. 11. $\hat{\mu}^2$ dependence of n_q/n_{SB} for $\beta = 0.70$ ($T/T_{c0} = 1.06$). The dots with error bars are the results of LQC$_2$D data, while the solid (dashed) line corresponds to the results of the PNJL model (the PNJL + baryon model). On the left (right) side of the thin dotted line, the system is in the C-phase (D-phase).

In QC_2D, the baryon is a boson consisting of two quarks. According to Refs. [19,20], the scalar baryon with the same degree of freedom as the PS meson has almost the same mass as the PS meson. Hence, we use the baryon mass $m_B = m_{ps} = 616$ MeV. The quark number density $n_{q,B}$ calculated with the baryon gas model is then obtained as

$$n_{q,B} = 2g \int \frac{d^3p}{(2\pi)^3} \left[\frac{1}{e^{\beta(E_B - 2\mu)} - 1} - \frac{1}{e^{\beta(E_B + 2\mu)} - 1} \right], \quad (36)$$

where $E_B = \sqrt{p^2 + {m_B}^2}$, $g = 3$ is the degree of freedom, and the factor 2 in front of g comes from the fact that the baryon is composed of two quarks. This modification improves agreement with LQC_2D particularly in the C-phase, but not in the D-phase. This implies that baryons disappear in the D-phase at least partially.

Figure 12 shows the same as Fig. 10 but for $\beta = 0.65$ ($T/T_{c0} = 0.96$). The system is in the C-phase on the left side of the thin dotted line, but in the D-phase on the right side. Again, the PNJL model undershoots LQC_2D in the C-phase, but the PNJL + baryon model almost reproduces the LQC_2D data in the C-phase, although the latter model overshoots LQC_2D data in the D-phase. Thus, the baryon may disappear in the D-phase.

More precisely, the PNJL + baryon model overestimates LQC_2D data also in the C-phase near the thin dotted line. This fact may imply that a repulsive force works between baryons there. It is well known that such a repulsive force suppresses the baryon number density in realistic nuclear matter.

Figure 13 shows the same as Fig. 10 but for $\beta = 0.60$ ($T/T_{c0} = 0.88$). The system is in the C-phase and the PNJL model largely underestimates LQC_2D data, but it is improved by the PNJL + baryon model. We can therefore conclude that baryon effects make an important contribution to n_q, whenever the system is in the C-phase.

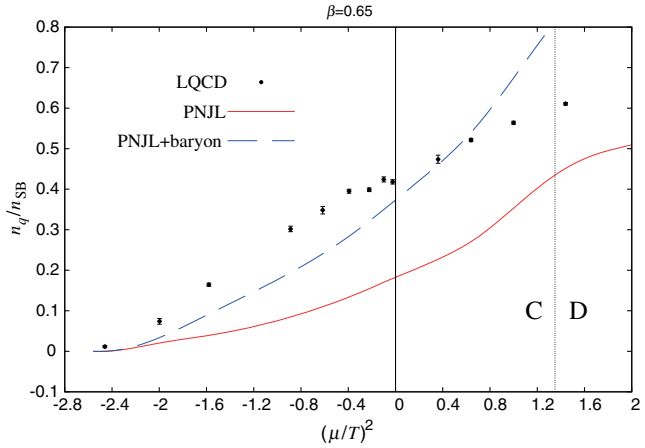

FIG. 12. $\hat{\mu}^2$ dependence of n_q/n_{SB} for $\beta = 0.65$ ($T/T_{c0} = 0.96$). For the definition of lines, see the Fig. 11 caption.

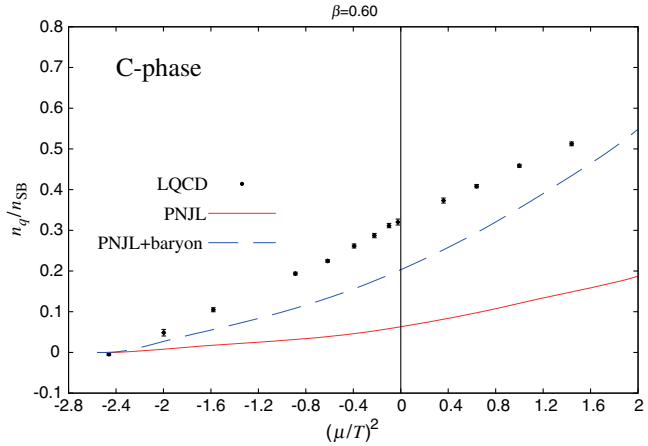

FIG. 13. $\hat{\mu}^2$ dependence of n_q/n_{SB} for $\beta = 0.60$ ($T/T_{c0} = 0.88$). For the definition of lines, see the Fig. 11 caption.

C. Chiral condensate

As mentioned in Sec. II C, the renormalization is necessary for the chiral condensate. The PNJL results are then simply multiplied by a normalization factor 1.92 so that the results can reproduce LQC_2D data at $\beta = 0.75$ ($T/T_{c0} = 1.18$) and $\hat{\mu}^2 = (i\pi/2)^2$. This choice of normalization is natural, since the PNJL model is a quark model and is expected to be more reliable at higher T.

Figure 14 shows $\hat{\mu}^2$ dependence of $\delta\sigma$ at $\beta = 0.75$ ($T/T_{c0} = 1.18$). At this temperature, the system is in the D-phase, and the PNJL model reproduces LQC_2D data well even at real μ.

Figures 15 and 16 show the $\hat{\mu}^2$ dependence of $\delta\sigma$ at $\beta = 0.70$ ($T/T_{c0} = 1.06$) and $\beta = 0.65$ ($T/T_{c0} = 0.96$),

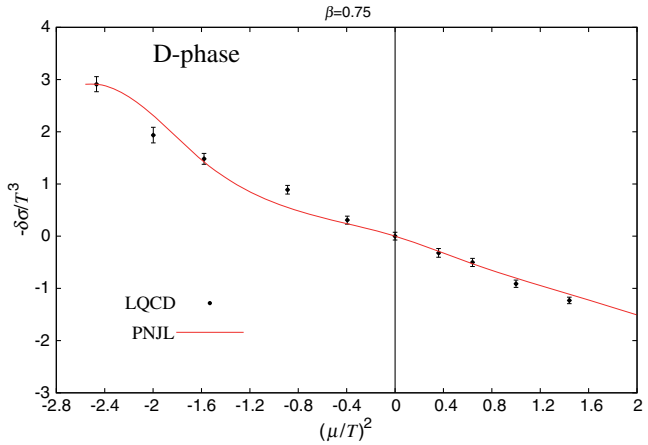

FIG. 14. $\hat{\mu}^2$ dependence of $\delta\sigma/T^3$ at $\beta = 0.75$ ($T/T_{c0} = 1.18$). The dots with error bars are the results of LQC_2D data, while the solid line corresponds to the results of the PNJL model. The PNJL results are multiplied by a normalization factor 1.92.

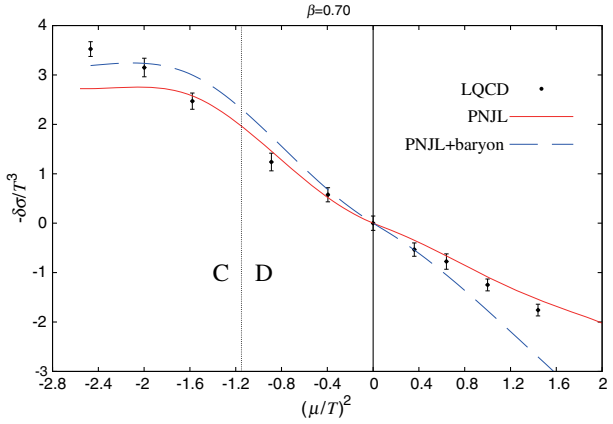

FIG. 15. $\hat{\mu}^2$ dependence of $\delta\sigma$ at $\beta = 0.70$ ($T/T_{c0} = 1.06$). The dots with error bars are the results of LQC_2D data, while the solid (dashed) line corresponds to the results of the PNJL (PNJL + baryon) model. The model results are multiplied by a normalization factor 1.92. The system is in the C-phase on the left side of the thin vertical dotted line, but in the D-phase on the right side.

respectively. On the left side of the thin vertical dotted line the system is in the C-phase, while it is in the D-phase on the right side. The PNJL model (solid line) is consistent with LQC_2D data in the D-phase, but not in the C-phase. In order to improve this disagreement in the C-phase, we add baryon effects to the PNJL model again:

$$\sigma_{\rm B} = \frac{\partial m_{\rm B}}{\partial m} g \int \frac{d^3p}{(2\pi)^3} \frac{m_{\rm B}}{E_{\rm B}} \left[\frac{1}{e^{\beta(E_{\rm B}-2\mu)}-1} + \frac{1}{e^{\beta(E_{\rm B}+2\mu)}-1} \right], \tag{37}$$

where we assume

$$\frac{\partial m_{\rm B}}{\partial m} = 2, \tag{38}$$

since a naive constituent quark model gives this value. As shown in Figs. 15 and 16, the PNJL + baryon model

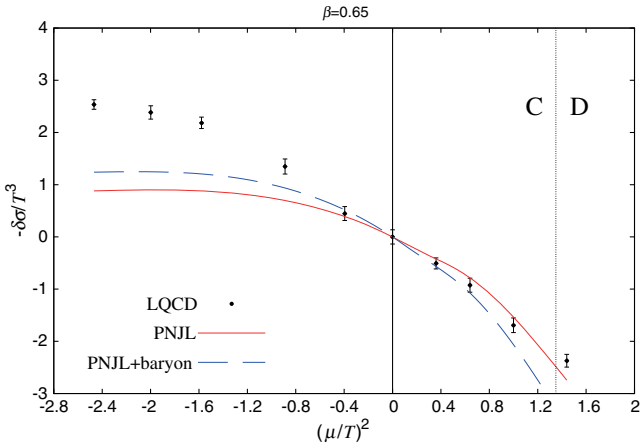

FIG. 16. $\hat{\mu}^2$ dependence of $\delta\sigma$ at $\beta = 0.65$ ($T/T_{c0} = 0.96$). For the definition of lines, see the Fig. 15 caption.

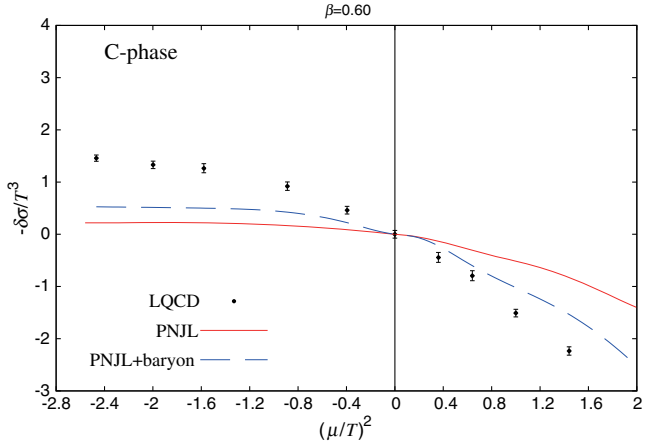

FIG. 17. $\hat{\mu}^2$ dependence of $\delta\sigma/T^3$ at $\beta = 0.60$ ($T/T_{c0} = 0.88$). For the definition of lines, see the Fig. 15 caption.

(dashed line) is more consistent with LQC_2D data than the PNJL model (solid line) in the C-phase, but less consistent in the D-phase. This means that baryon effects are significant only in the *C*-phase.

Figure 17 shows the $\hat{\mu}^2$ dependence of $\delta\sigma$ at $\beta = 0.60$ ($T/T_{c0} = 0.88$). At this temperature, the system is in the C-phase. The PNJL + baryon model (dashed line) yields better agreement with LQC_2D than the PNJL model (solid line) in the whole region of $\hat{\mu}^2$; note that $\delta\sigma$ is always zero at $\hat{\mu} = 0$ by the definition (12). Thus, baryon effects are important in the C-phase not only for $n_q/n_{\rm SB}$ but also for $\delta\sigma$.

D. Polyakov loop

Figure 18 shows the $\hat{\mu}^2$ dependence of Φ at $\beta = 0.75$. As mentioned in Sec. VA, the PNJL result is multiplied by a

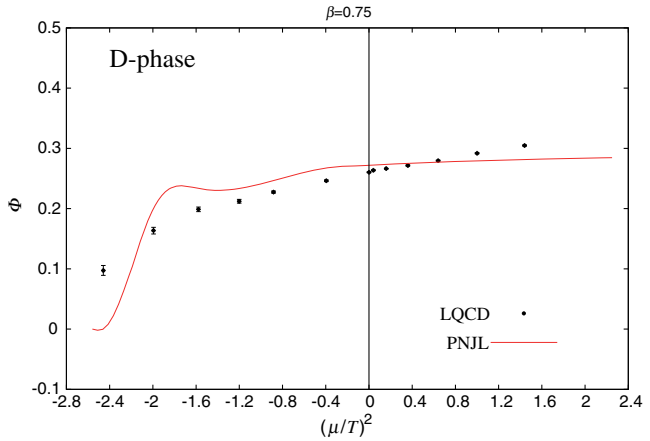

FIG. 18. $\hat{\mu}^2$ dependence of Φ at $\beta = 0.75$ ($T/T_{c0} = 1.18$). The dots with error bars show the results of the LQC_2D data, while the solid line corresponds to the results of the PNJL model. The PNJL results are multiplied by the normalization factor 0.304.

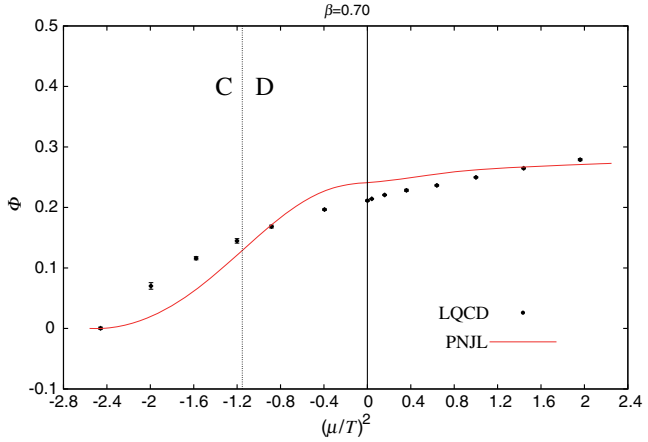

FIG. 19. $\hat{\mu}^2$ dependence of Φ at $\beta = 0.70$ ($T/T_{c0} = 1.06$). The dots with error bars show the results of the LQC$_2$D data, while the solid line shows the results of the PNJL model. The PNJL results are multiplied by the normalization factor 0.304. The system is in the C-phase on the left side of the thin vertical dotted line, while it is in the D-phase on the right side.

normalization factor 0.304 for Φ. At this temperature, the system is in the D-phase. The PNJL model (solid line) is consistent with the LQC$_2$D data except for the vicinity of the first-order RW transition.

Figures 19 and 20 show the $\hat{\mu}^2$ dependence of Φ at $\beta = 0.70$ and $\beta = 0.65$, respectively. The PNJL model deviates from LQC$_2$D data to some extent in the C-phase except for the point at $\hat{\mu}^2 = (i\frac{\pi}{2})^2$ where $\mathcal{C}Z_2$ symmetry restricts Φ to zero.

Figures 21 shows the $\hat{\mu}^2$ dependence of Φ at $\beta = 0.60$. At this temperature, the system is in the C-phase. The PNJL model deviates from LQC$_2$D data to some extent in the whole region except for the point at $\hat{\mu}^2 = (i\pi/2)^2$ where $\mathcal{C}Z_2$ symmetry restricts Φ to zero.

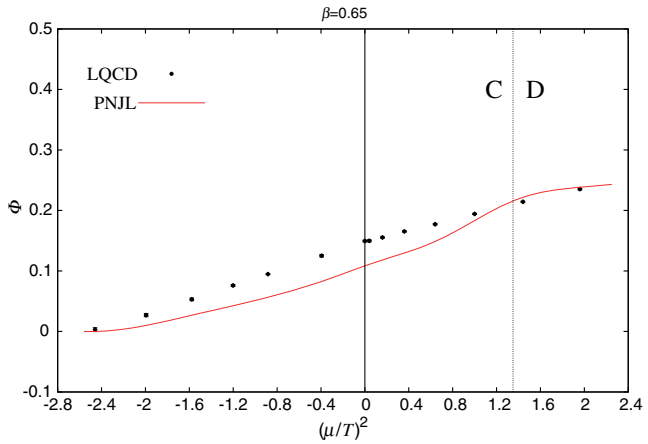

FIG. 20. $\hat{\mu}^2$ dependence of Φ at $\beta = 0.65$ ($T/T_{c0} = 0.96$). For the definition of lines, see the Fig. 19 caption.

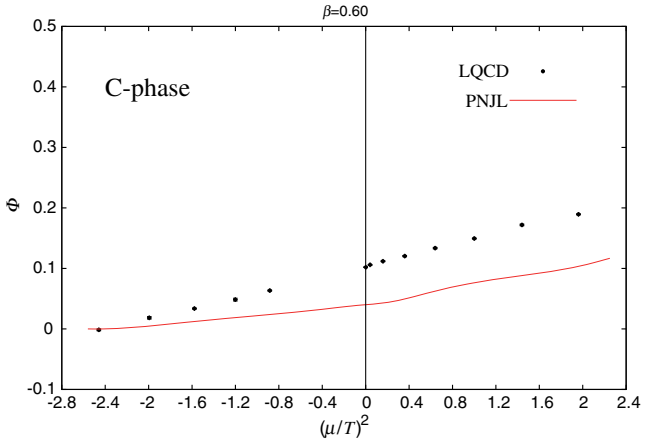

FIG. 21. $\hat{\mu}^2$ dependence of Φ at $\beta = 0.60$ ($T/T_{c0} = 0.88$). For the definition of lines, see the Fig. 18 caption.

Throughout all the analyses for Φ, we can say that the PNJL model cannot reproduce LQC$_2$D data properly in the vicinity of the RW transition and at lower T. A fine-tuning of $\mathcal{U}(\Phi)$ may be necessary to solve this problem.

E. Phase diagram

Figure 22 shows the phase diagram in the $\hat{\mu}^2$-T plane. The PNJL model (solid line) reproduces LQC$_2$D data well in the range of $\hat{\mu}^2 = -2 \sim 1$, but it overshoots LQC$_2$D data to some extent near the RW transition line and undershoots LQC$_2$D data in the large $\hat{\mu}^2$ region of $\hat{\mu}^2 \approx (1.2)^2$. It is an interesting question whether the PNJL model can reproduce LQC$_2$D data in the large $\hat{\mu}^2$ region as soon as the model is improved to reproduce LQC$_2$D data near the RW transition line.

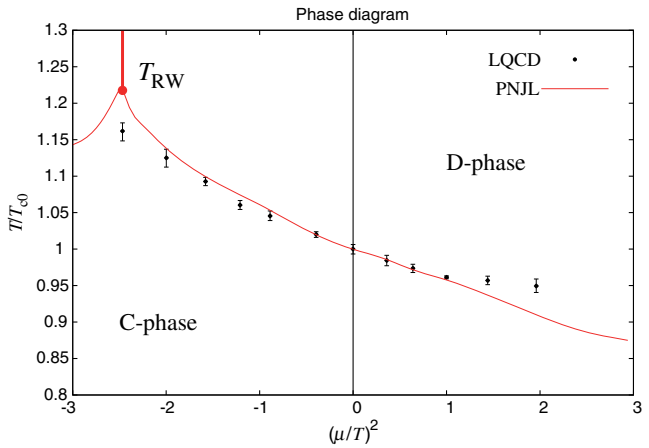

FIG. 22. Phase diagram in the $\hat{\mu}^2$-T plane. The dots with error bars represent the pseudocritical line of LQC$_2$D, while the solid line corresponds to the phase diagram of the PNJL model. The vertical thick solid line is the RW transition line determined with the PNJL model.

F. Errors and uncertainties in determination of the parameters of the PNJL model

In this section, we discuss errors and uncertainties in determination of the parameters of the PNJL model. First we estimate the effect of changing the value of G_v. Since the determination procedure of the PNJL model parameters is very complex, we concentrate our discussion on the last step of the parametrization. Suppose that, except for G_v, the parameters of the NJL sector of the PNJL model have already been determined to reproduce the vacuum properties and suppose that one of the undetermined four parameters, a, b, α, and G_v, have been eliminated by the condition $T_{c,\mathrm{PNJL}}(0) = T_{c,\mathrm{LQCD}}(0) = 146$ MeV; then we must fit the quark number density of the LQCD result at imaginary chemical potential and at $\beta = 0.75$ by choosing the remaining three parameters. Thus, the d.o.f. in the fitting is given by $N_{\mathrm{data}} - 3$, where N_{data} is the number of the LQCD data. The value of $\chi^2/\mathrm{d.o.f.}$ for this parametrization is shown in Table V. In the same table, the values of χ^2/N_{data} are also shown for the other LQCD observables. We see that the value of χ^2/N_{data} becomes very large at low temperature. The PNJL model cannot reproduce the LQCD data well when $\beta \neq 0.75$. In Table VI, the values of χ^2/N_{data} are shown for the quark number density and the chiral condensate at $\beta \neq 0.75$ when the PNJL + baryon model is used. We see that the value of χ^2/N_{data} becomes smaller in the C-phase while it becomes larger in the D-phase. This observation confirms our conclusion that the baryon contribution is important for these quantities in the C-phase and vanishes in the D-phase.

The χ^2 value may depend on the errors of the PNJL-model calculations. In order to obtain the σ that satisfies Eq. (25), we have searched for the solution with a step $\Delta\sigma = 0.08\sigma_0/I_\sigma$, where σ_0 is the value of the chiral condensate in vacuum and the integer I_σ is introduced to control the value of $\Delta\sigma$. Comparing the result of $I_\sigma = 10$ with that of $I_\sigma = 50$ in Tables V–VIII, we can find that the χ^2 value does not depend strongly on the errors of PNJL model calculations.

In Sec. V B, Fig. 10 showed the quark number density at $\beta = 0.75$ obtained by the PNJL model with $G_v/G_0 = 0$ and 0.5 as well as $G_v = 0.15G_0$. The values of χ^2 for the LQCD observables are summarized in Tables VII and VIII when the PNJL model with $G_v/G_0 = 0$ and 0.5 is used, respectively. We see that the $\chi^2/\mathrm{d.o.f.}$ or χ^2/N_{data} is considerably larger than that of the PNJL model with $G_v = 0.15G_0$. On the other hand, the values of $\chi^2/\mathrm{d.o.f.}$ or χ^2/N_{data} in the PNJL calculation with $G_v/G_0 = 0.1 \sim 0.4$ are not that much larger than those with $G_v/G_0 = 0.15$. Therefore, we conclude that G_v/G_0 is roughly estimated as $0.1 \sim 0.4$.

Next, we try to determine the PNJL parameters to reproduce the quark number density at lower temperature ($\beta = 0.60$) at the imaginary chemical potential instead of the one at $\beta = 0.75$. The left side of Fig. 23 shows the best fit we found for the quantity. In the new parameter set, $G_v = 0$ with the other parameters unchanged. In the figure, it is clear that the PNJL model results underestimate the LQCD results both in the imaginary and the real chemical potential regions (the right side of the figure) even if we use $G_v = 0$. The values of $\chi/\mathrm{d.o.f.}$ for quark number density at imaginary chemical potential and χ^2/N_{data} for quark number density at real chemical potential are 1973 and 4982, respectively. These values are much larger than those for the quark number density at $\beta = 0.75$ in Table V. We conclude that this parametrization is not relevant.

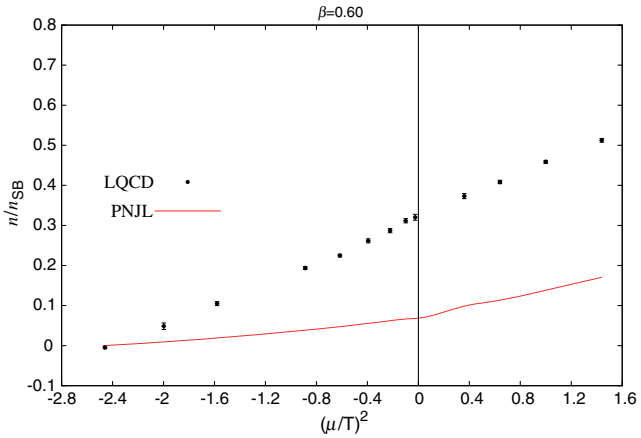

FIG. 23. $\hat{\mu}^2$ dependence of n_q/n_{SB} for $\beta = 0.60$ ($T/T_{c0} = 0.96$) with no vector-type interaction. For the definition of lines, see the Fig. 19 caption.

The PNJL model reproduces the μ dependence of the Polyakov-loop Φ only qualitatively. For example, in Fig. 18 the PNJL results underestimated Φ above $\mu/T > 0.5$ and overestimated at $\mu/T = 0 \sim 0.5$ in the real chemical potential region. It is very difficult to reproduce the μ dependence of the Polyakov loop more precisely in the present model. An additional *ad hoc* μ dependence of parameters of the effective model may explain the μ dependence of Φ but it violates thermodynamical consistency and fails to reproduce the other quantities such as quark number density. At present, it is an open question how we can reproduce the μ dependence of Φ precisely while the thermodynamical consistency is preserved.

VI. SUMMARY

We studied the phase structure of $\mathrm{QC_2D}$ at both real and imaginary μ by using an $8^3 \times 4$ lattice with the renormalization-group-improved Iwasaki gauge action [45,46] and the clover-improved two-flavor Wilson fermion action [47]. The Polyakov loop, the chiral condensate, and the quark number density were calculated at $0.86 \leq T/T_{c0} \leq 1.18$ and $-(\pi/2)^2 \leq \hat{\mu}^2 \leq (1.2)^2$. These quantities are smooth at $\hat{\mu} = 0$, as expected. This guarantees that the analytic

continuation of physical quantities from imaginary $\hat{\mu}$ to real $\hat{\mu}$ is possible.

Accuracy of the analytic continuation was tested in Refs. [25,26] with staggered fermions. In this paper we have made similar analyses with clover-improved Wilson fermions by assuming a polynomial series of $\hat{\mu}$ in the deconfinement phase and a Fourier series in the confinement phase, where coefficients of the series were determined at imaginary μ. As for the quark number density at $T/T_{c0} = 1.18$ corresponding to the deconfinement phase, the polynomial series up to $\hat{\mu}^3$ reproduces LQC_2D results well in the wide range of $0 \le \hat{\mu}^2 \le (1.2)^2$. At $T/T_{c0} = 0.88$ corresponding to the confinement phase, the results of the lowest-order Fourier series $\sin(2\theta)$ are consistent with LQC_2D results in the range of $0 \le \hat{\mu}^2 < 0.8$. At $T/T_{c0} = 0.96$ near the deconfinement transition, it is good only in $0 \le \hat{\mu}^2 < 0.4$. The analytic continuation is thus useful in the deconfinement and confinement regions, but less accurate in the transition region near $T/T_{c0} = 1$ where the deconfinement crossover takes place somewhere in the range of $-(\pi/2)^2 \le \hat{\mu}^2 \le (1.2)^2$ as $\hat{\mu}^2$ increases with T fixed. This is true for other quantities such as the Polyakov loop and the chiral condensate.

We have tested the validity of the PNJL model by comparing model results with LQC_2D ones, where the model parameters are fitted to the quark number density at $T/T_{c0} = 1.18$ and imaginary μ. As for the transition line of deconfinement crossover, the model results agree with those of LQC_2D. More precisely, the agreement is not perfect in the vicinity of the RW transition line and the large-$\hat{\mu}^2$ region of $(\hat{\mu})^2 \approx (1.2)^2$. It is interesting to examine whether the PNJL model can reproduce LQC_2D data in the large $\hat{\mu}^2$ region as soon as the model is improved to reproduce LQC_2D data near the RW transition line. A possible candidate for the improvement is a fine-tuning of the Polyakov-loop potential $\mathcal{U}(\Phi)$.

In the deconfinement region of $T/T_{c0} = 1.18$, the PNJL model yields good agreement with LQC_2D data at both real and imaginary μ for the quark number density, the chiral condensate, and the Polyakov loop. The agreement particularly at real μ indicates that the PNJL model is reliable in the deconfinement region. In the transition region of $T/T_{c0} \approx 1$, the agreement of the PNJL model with LQC_2D data is not perfect. As for the quark number density and the chiral condensate, however, the deviation can be reduced in the confinement area appearing at smaller $\hat{\mu}^2$ by introducing the baryon degree of freedom to the PNJL model. In the deconfinement area appearing at larger $\hat{\mu}^2$, on the contrary, the model overestimates LQC_2D results if the baryon contribution is taken into account. This means that baryons disappear at least partially in the deconfinement area. Also in the confinement region of $T/T_{c0} = 0.88$, the baryon degree of freedom is important. As for the Polyakov loop, the disagreement between PNJL and LQC_2D results in the confinement area cannot be solved by the baryon contribution. Of course, this comes from the fact that the Polyakov-loop potential is not changed by the baryon contribution in the present framework. The improvement of the PNJL model along this line is interesting.

The present analysis also shows that the vector-type four-quark interaction is necessary to explain LQC_2D data on the quark number density. This fact indicates also that in the realistic case of three colors the strength of the vector-type interaction can be determined from LQCD data at imaginary μ [39,43,44]. The present results indicate that the imaginary-μ matching approach [36] is a promising approach to the thermodynamics of QCD at finite real μ.

It should be stressed that our simulations were done on a small volume ($8^3 \times 4$). Therefore the finite volume effects are very strong and not eliminated completely by the normalization of physical quantities. There is the possibility that the PNJL model cannot reproduce the lattice data very well for this reason. Simulations using the larger lattice are needed to confirm our results.

In this paper, we consider only the μ region where the diquark condensate is expected to be zero. A quantitative check of our effective model in the larger μ region [20–22] would also be interesting.

ACKNOWLEDGMENTS

T. M. and H. K. thank H. Yoneyama, A. Sugiyama, and M. Tachibana for valuable comments. T. S., M. I., J. T., K. K., H. K., M. Y., and A. N. are/were supported by JSPS KAKENHI Grants No. 23749194, No. 27-3944, No. 25-3944, No. 26-1717, No. 26400279, No. 26400278, and Nos. 24340054 and 26610072, respectively. The numerical calculations were performed by using the NEC SX-9 and SX-ACE at CMC, Osaka University, and by using the RIKEN Integrated Clusters (RICC) facility.

APPENDIX: COEFFICIENTS OF FITTING FUNCTIONS FOR ANALYTIC CONTINUATION

We present the coefficients of analytic functions determined from LQC_2D data at imaginary μ and the χ^2/d.o.f. for the fitting. We also show the errors for the fitting by the PNJL model.

TABLE III. Coefficients of analytic functions and χ^2/d.o.f. for quark number density, chiral condensate, and the Polyakov loop at (a) $\beta = 0.75$, (b) $\beta = 0.70$, (c) $\beta = 0.65$, and (d) $\beta = 0.60$. The coefficients are determined from LQC_2D data at imaginary μ. The fitting range is $\hat{\mu}^2 = -1.15 \sim 0$ for (b) and $\hat{\mu}^2 = -(\pi/2)^2 \sim 0$ for the other cases.

(a)	$\beta = 0.75$				
Observable	Function	A	B	C	χ^2/d.o.f.
$\mathrm{Im}(n_q)$	Eq. (28)	3.61014(1466)	0.84703(2265)		2.914
$\mathrm{Im}(n_q)$	Eq. (29)	3.57904(1989)	0.70990(6347)	−0.08459(3657)	2.566
$\delta\sigma$	Eq. (26)	−0.07116(5561)	−1.07870(5010)		2.337
$\delta\sigma$	Eq. (27)	0.01304(8702)	−0.7336(0190)	0.1571(8106)	1.448
Φ	Eq. (26)	0.26153(70)	0.04379(12)		13.25
Φ	Eq. (27)	0.25994(73)	0.02410(310)	−0.01331(191)	4.534
(b)	$\beta = 0.70$				
Observable	Function	A	B	C	χ^2/d.o.f.
$\mathrm{Im}(n_q)$	Eq. (28)	3.32812(2089)	1.07313(5618)		1.077
$\mathrm{Im}(n_q)$	Eq. (29)	3.34986(2818)	1.2644(1755)	0.24168(21017)	1.016
$\delta\sigma$	Eq. (26)	0.00868(13029)	−1.39546(25909)		0.018
Φ	Eq. (27)	0.21241(112)	0.04621(279)		5.590
(c)	$\beta = 0.65$				
Observable	Function	A	B	C	χ^2/d.o.f.
$\mathrm{Im}(n_q)$	Eq. (34)	1.31566(759)			23.80
$\mathrm{Im}(n_q)$	Eq. (35)	1.44376(1216)	−0.11951(886)		4.075
$\delta\sigma$	Eq. (32)	1.1107(5784)	−1.33556(6933)		2.155
$\delta\sigma$	Eq. (33)	1.05958(6059)	−1.27686(7235)	0.19765(6969)	0.1933
Φ	Eq. (30)	0.15644(85)			7.920
Φ	Eq. (31)	0.15375(94)	−0.00461(68)		0.442
(d)	$\beta = 0.60$				
Observable	Function	A	B	C	χ^2/d.o.f.
$\mathrm{Im}(n_q)$	Eq. (34)	0.93599(80)			1.189
$\mathrm{Im}(n_q)$	Eq. (35)	0.94541(838)	−0.01438(74)		0.877
$\delta\sigma$	Eq. (32)	0.69931(3257)	−0.71395(3973)		0.2853
$\delta\sigma$	Eq. (33)	0.69633(3414)	−0.71059(4087)	0.01373(3913)	0.3394
Φ	Eq. (30)	0.10258(38)			3.826
Φ	Eq. (31)	0.10404(52)	−0.00195(46)		0.4438

TABLE IV. Coefficients of analytic functions and χ^2/d.o.f. for the pseudocritical line. The coefficients are determined from LQC_2D data at imaginary μ. The fitting range is $\hat{\mu}^2 = -(\pi/2)^2 \sim 0$ for all cases.

Function	A	B	C	χ^2/d.o.f.
Eq. (26)	0.66802(204)	−0.02868(167)		0.109
Eq. (27)	0.66871(257)	−0.02637(557)	0.00113(260)	0.089

TABLE V. χ^2/N for observables, where N is the number of d.o.f. for $\mathrm{Im}(n_q)$ at $\beta = 0.75$ and is the number of data for the other observables. The PNJL model with $G_\mathrm{v} = 0.15G_0$ is used for calculations. IM, RE, C, and D denote imaginary chemical potential region, real chemical potential region, confined phase (including the case with $\mu = 0$), and deconfined phase, respectively. See the text for the definition of I_σ.

β	n_q	$\delta\sigma$	Φ
$I_\sigma = 50$			
0.75 (IM)	6.201	0.7876	187.7
0.75 (RE)	2.190	1.949	169.0
0.70 (C)	106.3	10.25	76.86
0.70 (D)	279.9	1.588	460.4
0.65 (C)	1547	66.44	720.4
0.65 (D)	2132	12.20	43.49
0.60 (C)	2560	136.2	4664
$I_\sigma = 10$			
0.75 (IM)	7.088	0.819	188.4
0.75 (RE)	2.190	2.095	170.3
0.70 (C)	116.4	10.72	92.87
0.70 (D)	293.0	2.006	485.0
0.65 (C)	1581	73.26	653.7
0.65 (D)	2003	13.34	60.24
0.60 (C)	2450	136.2	4578

TABLE VI. χ^2/N_data for observables, where N_data is the number of data. The PNJL + baryon model is used for calculations. IM, RE, C, and D are the same as in Table V.

β	n_q	$\delta\sigma$
$I_\sigma = 50$		
0.70 (C)	47.60	3.875
0.70 (D)	5327	12.63
0.65 (C)	264.5	50.32
0.65 (D)	4932	113.1
0.60 (C)	329.0	64.03
$I_\sigma = 10$		
0.70 (C)	54.21	4.350
0.70 (D)	5291	11.73
0.65 (C)	188.3	44.30
0.65 (D)	5134	116.5
0.60 (C)	298.0	64.03

TABLE VII. χ^2/N for observables, where N is the number of d.o.f. for $\mathrm{Im}(n_q)$ at $\beta = 0.75$ and is the number of data for the other observables. The PNJL model with $G_\mathrm{v} = 0$ is used for calculations. IM, RE, C, and D are the same as in Table V.

β	n_q	$\delta\sigma$	Φ
$I_\sigma = 50$			
0.75 (IM)	41.08	0.4004	174.8
0.75 (RE)	260.4	0.2879	163.9
0.70 (C)	109.1	23.58	84.15
0.70 (D)	173.3	7.970	463.2
0.65 (C)	1496	1015	719.6
0.65 (D)	1630	14640	78.22
0.60 (C)	2559	3802	4615
$I_\sigma = 10$			
0.75 (IM)	40.89	0.4565	172.7
0.75 (RE)	263.6	0.4106	167.6
0.70 (C)	116.0	23.66	94.95
0.70 (D)	174.3	8.606	494.0
0.65 (C)	1385	996.5	641.4
0.65 (D)	1481	12870	108.9
0.60 (C)	2444	7555	4540

TABLE VIII. χ^2/N for observables, where N is the number of d.o.f. for $\mathrm{Im}(n_q)$ at $\beta = 0.75$ and is the number of data for the other observables. The PNJL model with $G_\mathrm{v} = 0.5G_0$ is used for calculations. IM, RE, C, and D are the same as in Table V.

β	n_q	$\delta\sigma$	Φ
$I_\sigma = 50$			
0.75 (IM)	41.23	3.482	214.3
0.75 (RE)	773.2	10.13	179.7
0.70 (C)	103.4	22.46	59.81
0.70 (D)	646.5	2.130	457.9
0.65 (C)	1660	798.2	734.7
0.65 (D)	3315	11220	1.746
0.60 (C)	2598	3421	4752
$I_\sigma = 10$			
0.75 (IM)	40.03	2.892	214.0
0.75 (RE)	773.2	12.76	181.5
0.70 (C)	77.67	18.43	21.32
0.70 (D)	653.1	2.639	490.5
0.65 (C)	1693	536.3	679.1
0.65 (D)	2994	10032	21.13
0.60 (C)	2472	6428	4691

[1] Z. Fodor and S. D. Katz, Phys. Lett. B **534**, 87 (2002).
[2] C. R. Allton, S. Ejiri, S. J. Hands, O. Kaczmarek, F. Karsch, E. Laermann, Ch. Schmidt, and L. Scorzato, Phys. Rev. D **66**, 074507 (2002).
[3] S. Ejiri Y. Maezawa N. Ukita S. Aoki T. Hatsuda N. Ishii K. Kanaya, and T. Umeda *et al.*, Phys. Rev. D **82**, 014508 (2010).
[4] P. de Forcrand and O. Philipsen, Nucl. Phys. **B642**, 290 (2002).

[5] M. D'Elia and M. P. Lombardo, Phys. Rev. D **67**, 014505 (2003).
[6] L. K. Wu, X. Q. Luo, and H. S. Chen, Phys. Rev. D **76**, 034505 (2007).
[7] M. D'Elia and F. Sanfilippo, Phys. Rev. D **80**, 111501 (2009).
[8] P. de Forcrand and O. Philipsen, Phys. Rev. Lett. **105**, 152001 (2010).
[9] K. Nagata and A. Nakamura, Phys. Rev. D **83**, 114507 (2011).
[10] J. Takahashi, K. Nagata, T. Saito, A. Nakamura, T. Sasaki, H. Kouno, and M. Yahiro, Phys. Rev. D **88**, 114504 (2013).
[11] J. Takahashi, H. Kouno, and M. Yahiro, Phys. Rev. D **91**, 014501 (2015).
[12] G. Aarts, Phys. Rev. Lett. **102**, 131601 (2009).
[13] G. Aarts, L. Bongiovanni, E. Seiler, D. Sexty, and I.-O. Stamatescu, Eur. Phys. J. A **49**, 89 (2013).
[14] D. Sexty, Phys. Lett. B **729**, 108 (2014).
[15] M. Cristoforetti, F. Di Renzo, and L. Scorzato, Phys. Rev. D **86**, 074506 (2012).
[16] H. Fujii, D. Honda, M. Kato, Y. Kikukawa, S. Komatsu, and T. Sano, J. High Energy Phys. 10 (2013) 147.
[17] A. Nakamura, Phys. Lett. B **149B**, 391 (1984).
[18] J. B. Kogut, D. K. Sinclair, S. J. Hands, and S. E. Morrison, Phys. Rev. D **64**, 094505 (2001).
[19] S. Muroya, A. Nakamura, and C. Nonaka, Phys. Lett. B **551**, 305 (2003).
[20] S. Hands, P. Sitch, and J.-I. Skullerud, Phys. Lett. B **662**, 405 (2008).
[21] S. Hands, S. Cotter, P. Giudice, and J. Skullerud, J. Phys. Conf. Ser. **432**, 012020 (2013).
[22] S. Cotter, J. Skullerud, P. Giudice, S. Hands, S. Kim, and D. Mehta, *Proc. Sci.*, LATTICE2012 (2012) 091 [arXiv:1210.6757]; S. Cotter, P. Giudice, S. Hands, and J. I. Skullerud, Phys. Rev. D **87**, 034507 (2013).
[23] T. Boz, S. Cotter, L. Fister, D. Mehta, and J.-I. Skullerud, Eur. Phys. J. A **49**, 87 (2013).
[24] P. Giudice and A. Papa, Phys. Rev. D **69**, 094509 (2004).
[25] P. Cea, L. Cosmai, M. D'Elia, and A. Papa, J. High Energy Phys. 02 (2007) 066.
[26] P. Cea, L. Cosmai, M. D'Elia, and A. Papa, Phys. Rev. D **77**, 051501(R) (2008).
[27] A. Roberge and N. Weiss, Nucl. Phys. **B275**, 734 (1986).
[28] K. Kashiwa, T. Sasaki, H. Kouno, and M. Yahiro, Phys. Rev. D **87**, 016015 (2013).
[29] P. N. Meisinger and M. C. Ogilvie, Phys. Lett. B **379**, 163 (1996).
[30] A. Dumitru and R. D. Pisarski, Phys. Rev. D **66**, 096003 (2002).
[31] K. Fukushima, Phys. Lett. B **591**, 277 (2004).
[32] S. K. Ghosh, T. K. Mukherjee, M. G. Mustafa, and R. Ray, Phys. Rev. D **73**, 114007 (2006).
[33] E. Megías, E. R. Arriola, and L. L. Salcedo, Phys. Rev. D **74**, 065005 (2006).
[34] C. Ratti, M. A. Thaler, and W. Weise, Phys. Rev. D **73**, 014019 (2006).
[35] S. Rößner, C. Ratti, and W. Weise, Phys. Rev. D **75**, 034007 (2007).
[36] K. Kashiwa, M. Matsuzaki, H. Kouno, Y. Sakai, and M. Yahiro, Phys. Rev. D **79**, 076008 (2009).
[37] Y. Sakai, K. Kashiwa, H. Kouno, and M. Yahiro, Phys. Rev. D **77**, 051901 (2008).
[38] H. Kouno, Y. Sakai, K. Kashiwa, and M. Yahiro, J. Phys. G **36**, 115010 (2009).
[39] Y. Sakai, K. Kashiwa, H. Kouno, M. Matsuzaki, and M. Yahiro, Phys. Rev. D **78**, 076007 (2008).
[40] K. Kashiwa, H. Kouno, M. Matsuzaki, and M. Yahiro, Phys. Lett. B **662**, 26 (2008).
[41] J. Sugano, J. Takahashi, M. Ishii, H. Kouno, and M. Yahiro, Phys. Rev. D **90**, 037901 (2014).
[42] T. Sasaki, N. Yasutake, M. Kohno, H. Kouno, and M. Yahiro, arXiv:1307.0681.
[43] Y. Sakai, K. Kashiwa, H. Kouno, M. Matsuzaki, and M. Yahiro, Phys. Rev. D **79**, 096001 (2009).
[44] K. Kashiwa, T. Hell, and W. Weise, Phys. Rev. D **84**, 056010 (2011).
[45] Y. Iwasaki, Nucl. Phys. B **B258**, 141 (1985).
[46] S. Itoh, Y. Iwasaki, and T. Yoshié, Phys. Lett. B **147B**, 141 (1984).
[47] B. Sheikholeslami and R. Wohlert, Nucl. Phys. **B259**, 572 (1985).
[48] S. Aoki, G. Boyd, R. Burkhalter, S. Hashimoto, N. Ishizuka, Y. Iwasaki, K. Kanaya, T. Kaneko, Y. Kuramashi, M. Okawa, A. Ukawa, and T. Yoshié, Phys. Rev. D **60**, 114508 (1999).
[49] G. P. Lepage and P. B. Mackenzie, Phys. Rev. D **48**, 2250 (1993).
[50] Y. Iwasaki, arXiv:1111.7054.
[51] W. Pauli, Nuovo Cimento **6**, 204 (1957).
[52] W. Pauli, Nuovo Cimento **7**, 411 (1958).
[53] T. Brauner, K. Fukushima, and Y. Hidaka, Phys. Rev. D **80**, 074035 (2009).
[54] N. Strodthoff, B.-J. Schaefer, and L. von Smekal, Phys. Rev. D **85**, 074007 (2012); N. Strodthoff and L. von Smekal, Phys. Lett. B **731**, 350 (2014).
[55] Y. Sakai, T. Sasaki, H. Kouno, and M. Yahiro, Phys. Rev. D **82**, 076003 (2010).
[56] Y. Aoki, G. Endrődi, Z. Fodor, S. D. Katz, and K. K. Szabó, Nature (London) **443**, 675 (2006).
[57] M. P. Lombardo, *Proc. Sci.*, LAT2005 (2006) 168 [arXiv:hep-lat/0509181].
[58] Y. Sakai, T. Sasaki, H. Kouno, and M. Yahiro, J. Phys. G **39**, 035004 (2012).